

Gaseous Spiral Structure and Mass Drift in Spiral Galaxies

Yonghwi Kim^{1*} and Woong-Tae Kim^{1,2†}

¹*Center for the Exploration of the Origin of the Universe (CEOU), Astronomy Program, Department of Physics & Astronomy, Seoul National University, Seoul 151-742, Republic of Korea*

²*Center for Theoretical Physics (CTP), Seoul National University, Seoul 151-742, Republic of Korea*

Accepted for publication in the MNRAS.

ABSTRACT

We use hydrodynamic simulations to investigate nonlinear gas responses to an imposed stellar spiral potential in disk galaxies. The gaseous medium is assumed to be infinitesimally thin, isothermal, and unmagnetized. We consider various spiral-arm models with differing strength and pattern speed. We find that the extent and shapes of gaseous arms as well as the related mass drift rate depend rather sensitively on the arm pattern speed. In models where the arm pattern is rotating slow, the gaseous arms extend across the corotation resonance (CR) all the way to the outer boundary, with a pitch angle slightly smaller than that of the stellar counterpart. In models with a fast rotating pattern, on the other hand, spiral shocks are much more tightly wound than the stellar arms, and cease to exist in the regions near and outside the CR where $\mathcal{M}_\perp / \sin p_* \gtrsim 25\text{--}40$, with \mathcal{M}_\perp denoting the perpendicular Mach number of a rotating gas relative to the arms with pitch angle p_* . Inside the CR, the arms drive mass inflows at a rate of $\sim 0.05\text{--}3.0 M_\odot \text{ yr}^{-1}$ to the central region, with larger values corresponding to stronger and slower arms. The contribution of the shock dissipation, external torque, and self-gravitational torque to the mass inflow is roughly 50%, 40%, and 10%, respectively. We demonstrate that the distributions of line-of-sight velocities and spiral-arm densities can be a useful diagnostic tool to distinguish if the spiral pattern is rotating fast or slow.

Key words: galaxies: ISM – galaxies: kinematics and dynamics – galaxies: structure – galaxies: nuclei – galaxies: spiral – hydrodynamics – ISM: general – shock waves

1 INTRODUCTION

Disk galaxies possess prominent non-axisymmetric features such as spiral arms and bars that have profound influences on galactic evolution in various ways (e.g., Buta & Combes 1996; Kormendy & Kennicutt 2004; Buta 2013; Sellwood 2013 and references therein). Stellar spiral arms not only trigger or organize star formation in the outer parts of disk galaxies but also drive secular changes in the orbits of stars and gas clouds, redistributing the mass in the disks (e.g., Lin & Shu 1964, 1966; Toomre 1964; Elmegreen 1995; Bertin & Lin 1996; Foyle et al. 2010). Bar potentials also affect the mass redistributions in the inner parts and are responsible for the formation of various gaseous substructures such as dust lanes and nuclear rings (e.g., Sanders & Huntley 1976; Athanassoula 1992; Heller & Shlosman 1994; Piner et al. 1995; Buta & Combes 1996; Kim et al. 2012a). Understanding the gravitational interaction of the stellar potentials with a gaseous medium is

therefore the first step to understand star formation, secular evolution, and morphological changes occurring in disk galaxies.

Among various secular processes, an angular momentum exchange between gas and a stellar pattern is particularly interesting since it leads to overall gas inflows or outflows in the radial direction. In barred galaxies, it has been well established that a non-axisymmetric torque exerted by a bar potential produces a pair of dust lanes in the gaseous medium, across which the gas loses angular momentum and falls radially inward to form a nuclear ring (e.g., Athanassoula 1992; Piner et al. 1995; Englmaier & Gerhard 1997; Patsis & Athanassoula 2000; Maciejewski 2004; Ann & Thakur 2005; Thakur et al. 2009; Kim et al. 2012a; Kim & Stone 2012), potentially powering star burst activities in nuclear rings as well as fueling active galactic nuclei (e.g. Shlosman et al. 1990; Regan & Mulchaey 1999; Knapen et al. 2000; Laurikainen et al. 2004; Jogee et al. 2005; Hunt et al. 2008; van de Ven & Fathi 2010). In particular, Kim et al. (2012b) demonstrated that the location of nuclear rings is determined not by the resonances but by the centrifugal barrier that the inflowing gas cannot over-

* e-mail : kimyh@astro.snu.ac.kr

† e-mail : wkim@astro.snu.ac.kr

come. This suggests that nuclear rings are smaller in size in more strongly-barred galaxies, entirely consistent with the observational results of Comerón et al. (2010).

Compared to the cases with a bar potential, the effects of a spiral potential on the gaseous structures and radial mass inflow are relatively poorly understood. While interactions of stellar density waves with stars and the associated stellar heating and radial migration have been a subject of intense study (e.g., Lynden-Bell & Kalnajs 1972; Donner & Thomasson 1994; Zhang 1996; Athanassoula 2002; Sellwood & Binney 2002; Roškar et al. 2008; Oh et al. 2008; Sellwood 2011; Brunetti et al. 2011; see also Kormendy & Kennicutt 2004 and Sellwood 2013 and references therein), only a few studies have explored angular momentum loss of gas due to the density waves (e.g., Kalnajs 1972; Roberts & Shu 1972; Lubow et al. 1986; Hopkins & Quataert 2011). For example, Roberts & Shu (1972) considered non-self-gravitating galactic spiral shocks and showed that the damping timescale of stellar density waves due to the angular momentum exchange is of the order of ~ 1 Gyr. Lubow et al. (1986) included the back reaction of the density waves on the gas density distribution, finding that the gas accretion rate due to the stellar pattern amounts to $\dot{M} \sim -(0.2-0.4) M_{\odot} \text{ yr}^{-1}$ for parameters representing the solar neighborhood in the Milky Way. These values of \dot{M} are overall consistent with the mass inflows inferred from chemical modeling in the Milky Way (Lacey & Fall 1985) and also those in external galaxies based on gravitational torque analyses (Haan et al. 2009; García-Burillo et al. 2009). Hopkins & Quataert (2011) used the epicycle approximation to derive an analytic expression for \dot{M} due to a non-axisymmetric potential.

While the derivations of \dot{M} by Lubow et al. (1986) and Hopkins & Quataert (2011) are insightful, they utilized a few notable approximations. First, Lubow et al. (1986) considered local, tightly-wound waves in both the stellar and gaseous media and ignored the self-gravitational torque on the gas in evaluating \dot{M} . They also included shear viscosity to represent cloud collisions, which tends to smear out shock profiles and thus makes it difficult to isolate the sole effect of the shock (e.g., Kim & Ostriker 2007; Kim et al. 2008). On the other hand, Hopkins & Quataert (2011) used the orbit crossing of test particles as a criterion for the shock formation, without considering the effects of gas pressure as well as the speed of incident flows relative to the pattern. Although Hopkins & Quataert (2011) showed that their \dot{M} is in good agreement with their numerical results for galaxies with a dominant bar-like potential, it is uncertain whether the same holds true for spiral galaxies in which the effects of thermal and ram pressures are more important than in barred galaxies.

Since dynamics involved with spiral arms is intrinsically nonlinear, it is desirable to run numerical hydrodynamic simulations in order to measure the mass drift rates driven by spiral arms properly. There have been numerous studies for gas responses to an imposed spiral potential, focusing on morphological changes of gaseous arms depending on the pattern speed (e.g., Patsis et al. 1994, 1997; Gómez & Cox 2002; Slyz et al. 2003; Yáñez et al. 2008; Gómez et al. 2013), formation of arm substructures such as branches, spurs, and feath-

ers (e.g., Chakrabarti et al. 2003; Wada & Koda 2004; Shetty & Ostriker 2006; Dobbs & Bonnell 2006; see also local models of Kim & Ostriker 2002, 2006), or star formation occurring in spiral arms (e.g., Shetty & Ostriker 2008; Wada 2008; Wada et al. 2011; Dobbs et al. 2011). While the arm-driven mass inflows might have affected the simulation outcomes in the work mentioned above, its rate has yet to be evaluated to assess its dynamical consequences on secular evolution quantitatively.

In this paper, we run global hydrodynamic simulations for gas evolution in galaxies with spiral potentials. We consider an infinitesimally-thin, uniform gaseous disk. We take an isothermal equation of state for the gas, and ignore the effect of radiative cooling and heating, star formation, and magnetic fields. Two important parameters characterizing a spiral pattern are its angular frequency Ω_p and strength \mathcal{F} , which are difficult to constrain observationally. Thus we in this work vary Ω_p and \mathcal{F} as free parameters to model spiral arms in various galactic situations, and study how \dot{M} depends on them. We will also compare our numerical results with the analytic expression presented in Hopkins & Quataert (2011).

In addition to evaluating \dot{M} , our models are also useful to address important issues related to the spatial extent, structures, and pitch angles of gaseous arms in comparison with their stellar counterparts. While the theory for spiral density waves suggests that the *stellar* pattern extends up to the corotation resonance (CR) or to the outer Lindblad resonance (OLR) if it is in the linear-regime (e.g., Toomre 1981; Lin & Lau 1979; Bertin et al. 1989a,b; Zhang 1996) and to the 4/1 resonance if it is strong enough to be nonlinear (Contopoulos & Grosbøl 1986, 1988; Patsis et al. 1991), it is uncertain whether the termination of *gaseous* arms corresponds to the resonance radii. Moreover, Gittins & Clarke (2004) showed using both semi-analytic and numerical approaches that gaseous arms are in general more tightly wound than the stellar arms. Although large uncertainties surround observational determinations of arm pitch angles, recent studies show that they are, statistically, slightly larger in the *I*- or *H*-band than in the *B*-band (Seigar et al. 2006; Davis et al. 2012; Martínez-García 2012), suggesting that the gaseous arms are likely more tightly wound than the stellar counterpart. We will show that the extent and pitch angles of gaseous arms are dependent somewhat sensitively upon the arm pattern speed. We will also show that the distributions of line-of-sight velocities in the projected galactic disk and density profiles of gaseous arms can be used to tell whether the observed arms are inside their CR or not.

The remainder of this paper is organized as follows. In Section 2, we describe the galaxy model and our choices of the model parameters, as well as the numerical method we use. In Section 3, we present the simulation results on morphologies of spiral shocks. In Section 4, we measure the arm-induced mass drift rates as functions of the pattern speed and strength of the stellar arms. In Section 5, we present the distributions of line-of-sight velocities in the plane of sky and discuss how they can be used to obtain information on the arm pattern speed. In Section 6, we conclude with a summary and discussion of our results and their astronomical implications.

2 MODEL AND METHOD

We consider an infinitesimally-thin, self-gravitating gaseous disk, and study its nonlinear responses to an imposed non-axisymmetric potential representing stellar spiral arms. The disk is assumed to be unmagnetized and isothermal, for simplicity. The basic equations of hydrodynamics expanded in the $z = 0$ plane corotating with the spiral potential are

$$\frac{\partial \Sigma}{\partial t} + \nabla \cdot (\Sigma \mathbf{u}) = 0, \quad (1)$$

$$\frac{\partial \mathbf{u}}{\partial t} + (\mathbf{u} \cdot \nabla) \mathbf{u} = -\frac{c_s^2}{\Sigma} \nabla \Sigma - \nabla (\Phi_{\text{ext}} + \Phi_{\text{gas}}) + \Omega_p^2 \mathbf{R} - 2\Omega_s \times \mathbf{u}, \quad (2)$$

$$\nabla^2 \Phi_{\text{gas}} = 4\pi G f(z) \Sigma, \quad (3)$$

where Σ is the gas surface density, \mathbf{u} is the velocity in the rotating frame, c_s is the isothermal speed of sound, $\Omega_p = \Omega_p \hat{z}$ is the pattern speed of the spiral arms, and Φ_{ext} and Φ_{gas} denote the external gravitational potential and self-gravitational potential, respectively. In equation (3), the function $f(z)$ is introduced to account for the dilution of self-gravity at the disk mid-plane due to finite disk thickness: we take a Gaussian profile with thickness of $H = 0.1R$ (Shetty & Ostriker 2008). The velocity \mathbf{v} in the inertial frame is obtained from $\mathbf{v} = \mathbf{u} + R\Omega_p \hat{\phi}$.

2.1 Galaxy Model

The external gravitational potential consists of an axisymmetric component and a non-axisymmetric spiral component Φ_{sp} . The static axisymmetric part responsible for galaxy rotation is comprised of a stellar disk, a spherical bulge/ halo, and a central black hole with mass $M_{\text{BH}} = 4 \times 10^7 M_{\odot}$, identical to that in Kim et al. (2012b). Figure 1 plots the resulting rotation curve, with a flat part with $v_c \simeq 200 \text{ km s}^{-1}$ over most of the disk plane and a rapidly rising part as $v_c \propto (M_{\text{BH}}/R)^{1/2}$ toward the center due to the presence of the black hole.

For the non-axisymmetric spiral potential, we take a trailing logarithmic-arm model of Shetty & Ostriker (2006):

$$\Phi_{\text{sp}}(R, \phi; t) = \Phi_0 \cos \left(m \left[\phi + \frac{\ln R}{\tan p_*} - \Omega_p t + \phi_0 \right] \right), \quad (4)$$

for $R \geq 2 \text{ kpc}$ (see also Roberts 1969). Here, m , p_* , Ω_p , and ϕ_0 denote the number, the pitch angle, the pattern speed, and the initial phase of the arms, respectively. Note that Φ_{sp} is tapered from $R = 2 \text{ kpc}$ to 1 kpc by a Gaussian function to have $\Phi_{\text{sp}} = 0$ at $R \leq 1 \text{ kpc}$. The amplitude of the spiral potential Φ_0 in equation (4) is controlled by the dimensionless parameter

$$\mathcal{F} \equiv \frac{m|\Phi_0|}{v_c^2 \tan p_*}, \quad (5)$$

which measures the gravitational force due to the spiral arms in the direction perpendicular to the arms relative to the radial force from the background axisymmetric potential (e.g., Roberts 1969; Kim & Ostriker 2002, 2006; Oh et al. 2008; Shetty & Ostriker 2008). We fix $m = 2$, $p_* = 20^\circ$, and $\phi_0 = 147^\circ$. We vary \mathcal{F} from 5 to 20% to study situations with differing arm strength.

It is quite challenging to measure the pattern

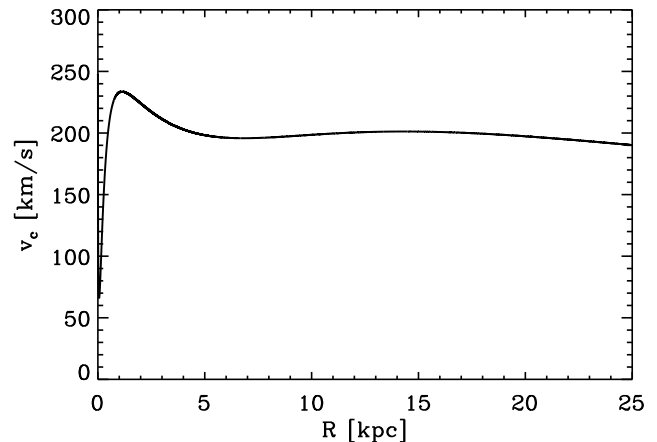


Figure 1. Rotational velocity v_c of our galaxy model as a function of the galactocentric radius R . Over much of the disk, $v_c \simeq 200 \text{ km s}^{-1}$, corresponding to a normal disk galaxy.

speeds of spiral arms. Self-consistent modeling of the Milky Way shows that stability and observed tangent points of the spiral arms are best described by $\Omega_p = 20 \text{ km s}^{-1} \text{ kpc}^{-1}$ (e.g., Amaral & Lépine 1997; Martos et al. 2004). On the other hand, analyses based on the Tremaine & Weinberg (1984)’s method indicate that the arms in external galaxies have pattern speeds in a wide range of $\Omega_p \sim 10\text{--}45 \text{ km s}^{-1} \text{ kpc}^{-1}$ (e.g., Zimmer et al. 2004; Fathi et al. 2009; Martínez-García et al. 2011). N -body simulations for the formation of non-axisymmetric features in disk galaxies also show that the angular frequency of spiral arms is diverse (e.g., Sellwood & Sparke 1988; Rautiainen & Salo 1999; Bournaud & Combes 2002; Roca-Fàbrega et al. 2013). Therefore, we in this paper consider three different cases: $\Omega_p = 30 \text{ km s}^{-1} \text{ kpc}^{-1}$ (fast arm models), $\Omega_p = 20 \text{ km s}^{-1} \text{ kpc}^{-1}$ (intermediate-speed arm models), and $\Omega_p = 10 \text{ km s}^{-1} \text{ kpc}^{-1}$ (slow arm models). In what follows, we refer to these as the F, I, and S models, respectively. The positions of the CR, the inner Lindblad resonance (ILR), and the 4/1 resonance are $R_{\text{CR}} = 6.5, 9.9, \text{ and } 19.8 \text{ kpc}$, $R_{\text{ILR}} = 2.5, 3.6, \text{ and } 6.0 \text{ kpc}$, and $R_{4/1} = 4.4, 6.4, \text{ and } 12.9 \text{ kpc}$ for the F, I, and S models, respectively.

We run 18 models that differ in \mathcal{F} , Ω_p , and the presence or absence of gaseous self-gravity. Table 1 lists the model parameters. The prefixes ‘‘F’’, ‘‘I’’, and ‘‘S’’ stand for the models with fast, intermediate-speed, and slow arms, while the postfixes ‘‘G’’ and ‘‘N’’ indicate self-gravitating and non-self-gravitating models, respectively. In all models, the gas sound speed is taken to $c_s = 10 \text{ km s}^{-1}$ that effectively includes a contribution of turbulent motions (e.g., McKee & Ostriker 2007). For models in which self-gravity is considered, Φ_{gas} is calculated by using the Kalnajs (1971) scheme described in Shetty & Ostriker (2008). All the models start from a gaseous disk with uniform surface density $\Sigma_0 = 10 M_{\odot} \text{ pc}^{-2}$. We take Models F10G, I10G, and S10G with $\mathcal{F} = 10\%$ as our fiducial models.

2.2 Numerical Methods

As in Kim et al. (2012b), we integrate equations (1)–(3) using the CMHOG code in cylindrical geometry. CMHOG is a

Table 1. Model Parameters

Model	\mathcal{F} (%)	Ω_s ($\text{km s}^{-1} \text{kpc}^{-1}$)	Self-gravity
F05G	5	30	included
F10G	10	30	included
F20G	20	30	included
I05G	5	20	included
I10G	10	20	included
I20G	20	20	included
S05G	5	10	included
S10G	10	10	included
S20G	20	10	included
F05N	5	30	omitted
F10N	10	30	omitted
F20N	20	30	omitted
I05N	5	20	omitted
I10N	10	20	omitted
I20N	20	20	omitted
S05N	5	10	omitted
S10N	10	10	omitted
S20N	20	10	omitted

grid-based code for ideal hydrodynamics based on the piecewise parabolic method in its Lagrangian remap formulation (Colella & Woodward 1984), which is third-order accurate in space (Piner et al. 1995). All the simulations are performed in a frame corotating with the arms. In the simulation domain, therefore, the spiral potential remains stationary. In order to avoid strong transients in the gas flows caused by a sudden introduction of the spiral potential, we increase its amplitude slowly over the timescale of 0.1 Gyr. We run the simulations until $t = 1$ Gyr, beyond which the numerical results are compromised by waves propagating from the outer radial boundary.

By assuming a reflection symmetry with respect to the galaxy center, the simulations are performed on a half-plane with $-\pi/2 \leq \phi \leq \pi/2$. We set up a logarithmically-spaced cylindrical grid over $R = 0.5$ kpc to 40 kpc, with 1102 radial and 790 azimuthal grid points. The corresponding grid spacing is $\Delta R = 2, 40,$ and 159 pc at the inner radial boundary, at $R = 10$ kpc, and at the outer radial boundary, respectively. We apply the continuous and outflow boundary conditions at the outer and inner radial boundaries, respectively, while adopting the periodic boundary conditions at the azimuthal boundaries. The gas moving in through the inner radial boundary is considered lost out of the simulation domain.

3 SPIRAL STRUCTURES

In this section, we focus on spiral structures induced by the imposed spiral potential. Radial mass flows associated with the spiral shocks will be presented in Section 4.

3.1 Overall Morphology

We begin by describing the temporal evolution of our fiducial models with $\mathcal{F} = 10\%$: the evolution of other models with different arm strength is qualitatively similar. Figure 2 plots snapshots of the gaseous surface density in logarithmic

scale at $t = 0.2, 0.4, 0.7,$ and 1.0 Gyr for the self-gravitating models. The left, middle, and right columns are for the F, I, and S models with $\Omega_p = 30, 20,$ and $10 \text{ km s}^{-1} \text{ kpc}^{-1}$, respectively. The spiral arms remain stationary in the simulation domain. The dotted circle in each panel marks the CR of the spiral arms, outside of which the gas is rotating in the clockwise direction relative to the spirals.

It is apparent that the spiral potential strongly perturbs the gas orbits, forming large-scale spiral shocks, although the regions affected by the potential depend on Ω_p . In the F and I models, spiral shocks are strong only inside the termination radius of $R_{\text{term}} \approx 17$ and 25 kpc, respectively, outside which small-amplitude perturbations propagating outward do not develop into shocks. On the other hand, the whole disk is strongly affected by the spiral potential to induce shocks in the S models. As we will show more quantitatively in Section 3.2.1 below, this is because the gas does not have sufficient time to respond to a spiral potential when it rotates too rapidly. In the F and I models, the outer ends of gaseous arms, which cannot be extended beyond R_{term} , curl back radially in and are loosely connected to the other arms at late time, producing a ring-like structure just inside R_{term} . These ring-like structures are more vividly evident in models with large p_* , as in models presented in Patsis et al. (1994). We defer a more detailed discussion on this issue to Section 6.2.

Figure 2 shows that the density snapshots at $t = 0.4$ Gyr of Models I10G and S10G contain weak gaseous structures, indicated by the arrows, developing from the arms near the 4/1 resonance.¹ They are continually generated from the 4/1 resonance due to the nonlinear effects (e.g., Contopoulos & Grosbøl 1986, 1988; Artymowicz & Lubow 1992), and propagate through the disk. These weak structures share a lot of similarities in appearance and in geometrical locations with “branches” and “spurs” identified by Chakrabarti et al. (2003) (see also Patsis et al. 1994, 1997; Yáñez et al. 2008). These terminologies of resonance features are visually motivated to indicate structures bifurcating from the main arms. Branches refer to trailing structures winding in the same sense as the main arms such as in Model I10G, whereas those leading the arms such as in Model S10G are termed spurs (Chakrabarti et al. 2003). We find that models with larger \mathcal{F} and/or smaller Ω_p tend to produce spurs more easily, while models with smaller \mathcal{F} and/or larger Ω_p are more likely to possess branches, consistent with the results of Chakrabarti et al. (2003). We note that bifurcations of gaseous arms in our models are much weaker than those reported in Patsis et al. (1994, 1997), owing to a small pitch angle. We have run additional models (not listed in Table 1) with pitch angles of $p_* = 33^\circ$ and 44° , and confirmed that arms with a large pitch angle indeed develop strong bifurcations. These results suggest that the growth of resonance features is highly sensitive to the arm parameters.

Figure 2 also shows that some parts of spiral shocks wiggle and form small clumps along them at late time. This clump-forming wiggle instability is more virulent when shocks are stronger. Yet, its physical nature is uncertain. Based on the Richardson criterion, Wada & Koda (2004)

¹ The 4/1 resonance corresponds to the first ultraharmonic resonance for 2-armed spirals (e.g., Chakrabarti et al. 2003).

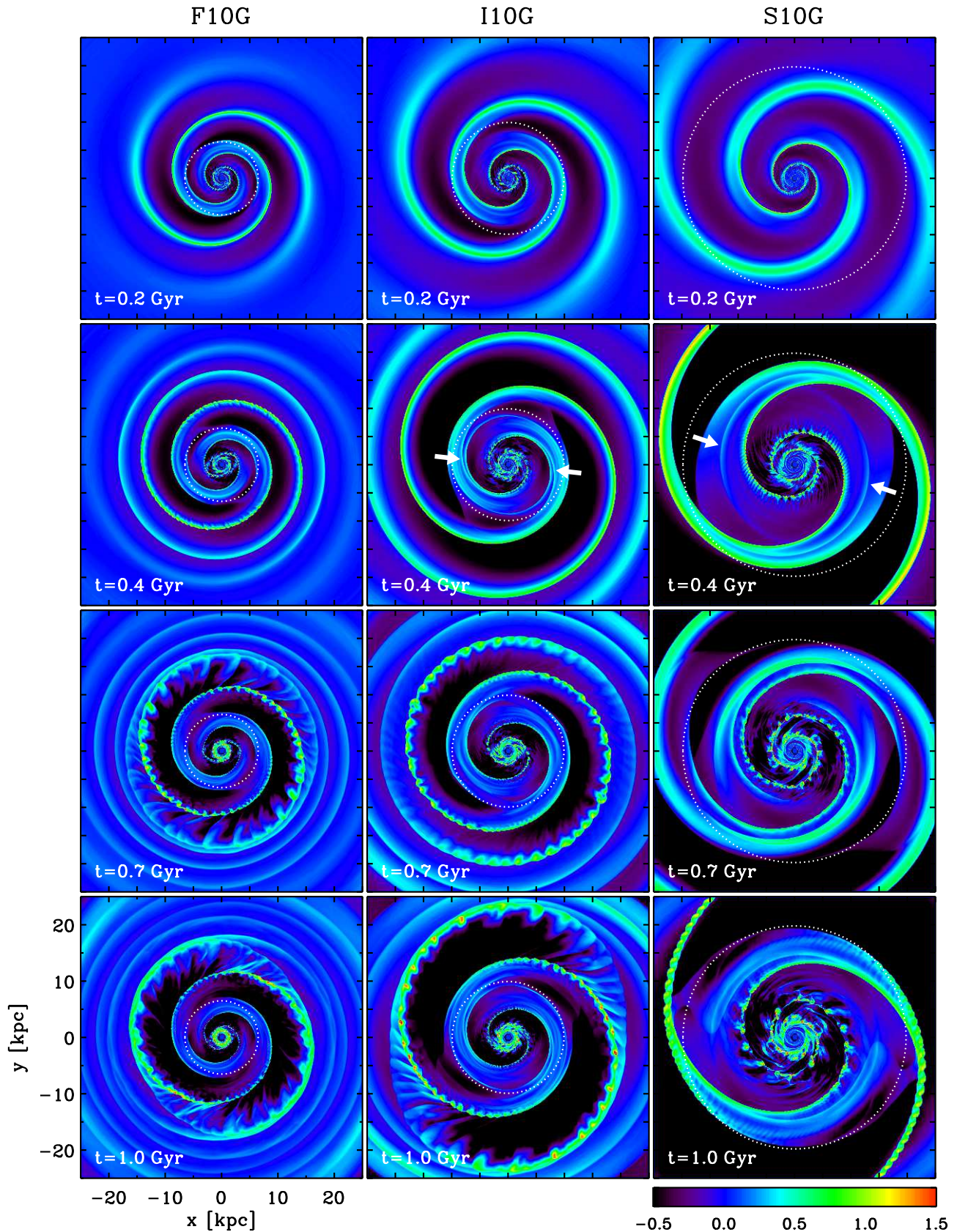


Figure 2. Snapshots of gas surface density in logarithmic scale for Models F10G, I10G, and S10G from left to right at $t = 0.2, 0.4, 0.7,$ and 1.0 Gyr from top to bottom. In each panel, the CR of the arms is indicated as a dotted circle. The white arrows in the $t = 0.4$ Gyr panels of Models I10G and S10G indicate weak structures emanating from the $4/1$ resonance. Colorbar labels $\log(\Sigma/\Sigma_0)$.

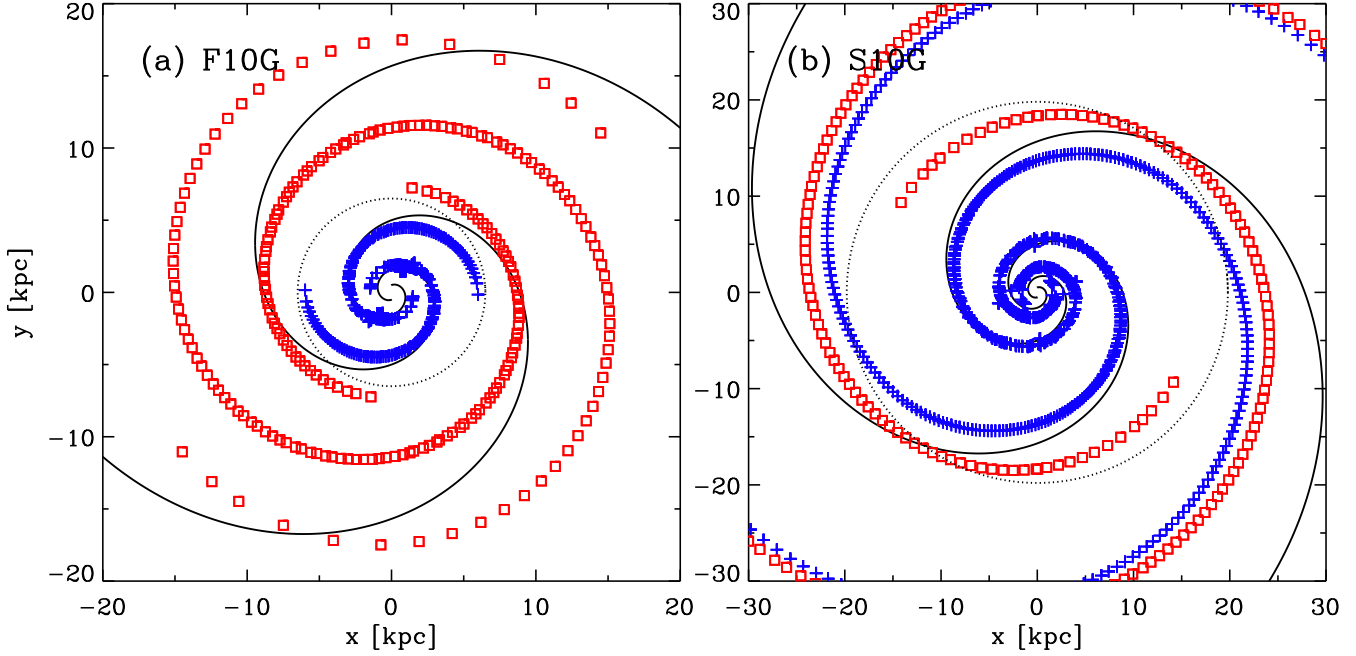


Figure 3. Locations (symbols) of spiral shocks in Models F10G and S10G at $t = 0.4$ Gyr. Pluses and squares indicate the shocks produced primarily by the gas inside and outside the CR, respectively. The solid lines draw the loci of the spiral potential minima, while the dotted circle marks the CR of the spiral pattern.

argued that it is the Kelvin-Helmholtz instability of a shear layer behind the shock, although the expanding radial velocity after the shock has a local stabilizing effect (Dwarkadas & Balbus 1996). Dobbs & Bonnell (2006) interpreted the clump formation as orbit crowding of gaseous particles that change their angular momenta in the shock. Kim et al. (2012a) suggested that vorticity at the curved shocks increases secularly due to Crocco’s theorem, producing clumps in the nonlinear stage. On the other hand, it cannot be ruled out the possibility that the wiggle instability can be of a numerical origin, caused by the inability of a numerical method to properly resolve a shock inclined to numerical grids (Hanawa & Kikuchi 2012). As Figure 2 shows, the wiggle instability develops only in the regions well away from the CR, since its growth requires strong shocks (Wada & Koda 2004; Kim & Ostriker 2006). The wiggle instability is weaker in models with a lower pattern speed, which is most likely due to the fact that large gas velocities relative to the spiral potential in the simulation domain have considerable numerical viscosity (e.g., Kim et al. 2008), tending to suppress the wiggle instability.² We note that regardless of its nature, the wiggle instability occurring on small scale does not significantly affect the radial gas drift rate averaged both azimuthally and temporally.

Gas self-gravity does not make significant differences in the overall arm morphologies, since our initial disk has the Toomre stability parameter

² We find that spiral shocks in models with parameters identical to those of Models F10G and S10G calculated in the inertial frame rather than in the rotating frame are stable to the wiggle instability, indirectly demonstrating stabilization by numerical viscosity.

$$Q_T = \frac{\kappa c_s}{\pi G \Sigma} \approx 2.1 \left(\frac{R}{10 \text{ kpc}} \right)^{-1} \left(\frac{\Sigma}{10 M_\odot \text{ pc}^{-2}} \right)^{-1}, \quad (6)$$

which is larger than unity at $R \lesssim 20$ kpc. Here κ denotes the epicycle frequency. Although $Q_T < 1$ in the outer regions, Figure 2 shows that gravitational instability does not manifest itself presumably due to the effect of finite disk thickness in solving the Poisson equation (3).

3.2 Spiral Shocks

3.2.1 Structure

A global stellar spiral pattern that persists throughout the disk perturbs gas orbits that would otherwise remain circular, and produces spiral shocks in the gas flows. To measure the strength of spiral shocks, we define the dimensionless compression factor

$$\alpha \equiv -(\nabla \cdot \mathbf{v}) \Delta R / c_s, \quad (7)$$

(e.g., Maciejewski 2004; Thakur et al. 2009; Kim et al. 2012a). For steady isothermal shocks in planar geometry, $\alpha = \mathcal{M}_\perp - 1/\mathcal{M}_\perp$, where \mathcal{M}_\perp is the Mach number of the incident flows perpendicular to the shock fronts. Thus, any positive value of α should correspond to shocks if the flows are one-dimensional and in steady state. However, the gas flows in the disk are two-dimensional and are not completely steady. We empirically found that shock fronts (i.e., discontinuities in density and velocities) in our models are well identified by the condition $\alpha \gtrsim 0.5$. In what follows, we thus impose $\alpha \geq 0.5$ as a condition for the presence of spiral shocks.

To delineate the positions and shapes of the spiral shocks, Figure 3 plots as plus and square symbols the loci

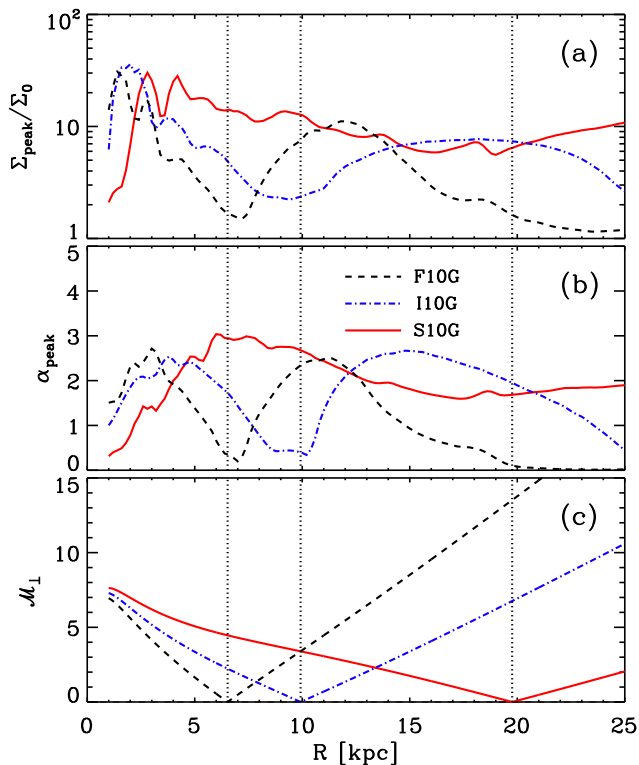


Figure 4. Radial dependence of (a) the peak density $\Sigma_{\text{peak}}/\Sigma_0$, (b) the maximum compression factor α_{peak} , and (c) the perpendicular Mach number \mathcal{M}_\perp for Models F10G (dashed), I10G (dot-dashed), and S10G (solid) at $t = 0.4$ Gyr. The vertical dotted lines at $R = 6.5$ kpc, 9.9 kpc, and 19.8 kpc mark the CR of the arms in the F, I, and S models, respectively.

of the maximum α (≥ 0.5) at each R for Models F10G and S10G at $t = 0.4$ Gyr. In each panel, the dotted circle indicates the CR of the arms, while the black solid curves mark the loci of the spiral potential minima. It is apparent that spiral shocks in Model S10G are located relatively close (within $\sim 20^\circ$ in ϕ) to the potential minima, while they do not follow the spiral potential closely in Model F10G. Figure 4 plots the radial variations over $1 \text{ kpc} \leq R \leq 25 \text{ kpc}$ of the peak density Σ_{peak} , the peak compression factor α_{peak} , and the perpendicular Mach number $\mathcal{M}_\perp = R|\Omega - \Omega_p| \sin p_*/c_s$ of the incident flows relative to the arms for our standard models at $t = 0.4$ Gyr. The vertical dotted lines mark the CR of the arms in the F, I, and S models. Note that Σ_{peak} is smaller near the respective CR than the other shocked regions in all models.

The extent of spiral shocks depends sensitively on the pattern speed of the spiral pattern as well as its strength. To produce quasi-steady spiral shocks, the gas has to not only move faster than the local sound speed relative to the perturbing potential, but also have sufficient time to respond to one arm before encountering the next arm. In Model F10G, the spiral shocks exist only at $R \lesssim R_{\text{term}} = 17$ kpc where $\mathcal{M}_\perp \lesssim 12$ (Fig. 4c). In Models F05G and F20G, they extend up to $R_{\text{term}} = 15$ kpc with $\mathcal{M}_\perp = 10$ and to $R_{\text{term}} = 21$ kpc with $\mathcal{M}_\perp = 15$, respectively. In the I models, the termination radii of spiral shocks are $R_{\text{term}} = 22$, 25 , and 32 kpc for $\mathcal{F} = 5$, 10 , and 20% , respectively. The time interval

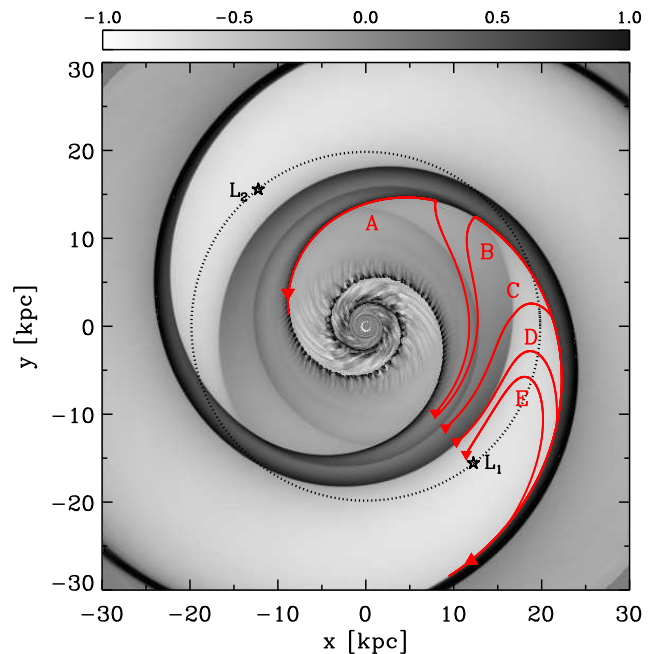


Figure 5. A few instantaneous streamlines of the gas, starting from near the Lagrangian point L_1 , in Model S10G at $t = 0.4$ Gyr in the frame corotating with the spiral potential. L_2 is another Lagrangian point at the opposite side. The dotted circle denotes the position of the CR. The streamline marked by “A” hits the shock at an oblique angle less than 90° and bends radially inward downstream, while the other streamlines meet the shocks at angles larger than 90° and thus move radially outward after the shocks. Grayscale bar labels $\log(\Sigma/\Sigma_0)$.

between two successive passages of the spiral potential is $t_{\text{arm}} = \pi/|\Omega - \Omega_p|$, while the arm-to-arm crossing time of sound waves is $t_{\text{sound}} = \pi R/c_s$. Thus the condition for the formation of quasi-steady spiral shocks can be written as

$$\frac{t_{\text{sound}}}{t_{\text{arm}}} = \frac{\mathcal{M}_\perp}{\sin p_*} \lesssim 20 + 100\mathcal{F}, \quad (8)$$

for $5\% \leq \mathcal{F} \leq 20\%$, insensitive to the arm pattern speed. If this condition is not satisfied, the gas does not properly feel the azimuthal variations of the imposed potential that is rotating too rapidly. This is consistent with the finding of Baker & Barker (1974) that gas with too large an entry velocity relative to the arms moves almost ballistically, without producing a steady-state shock. In the S models, the entire simulation domain has $\mathcal{M}_\perp/\sin p_* \lesssim 20$, and thus quasi-steady spiral shocks form over the whole disk.

A conventional wisdom is that spiral shocks are absent in the CR region where $\mathcal{M}_\perp = 0$. However, Figure 3b reveals that spiral shocks, albeit somewhat weak, are not completely absent near the CR in the S models. There are two different kinds of spiral shocks depending on the locations. The first kind, marked by plus symbols, starting from the ILR is produced primarily by the gas inside the CR that is rotating faster than the spiral potential. In Model S10G, these spiral shocks become weaker with increasing R owing to the decrease in \mathcal{M}_\perp and move across the CR located at $R_{\text{CR}} = 19.8$ kpc, extending all the way to the outer radial boundary. In Models F10G and I10G, however, they barely extend across the respective CR. The second kind, marked

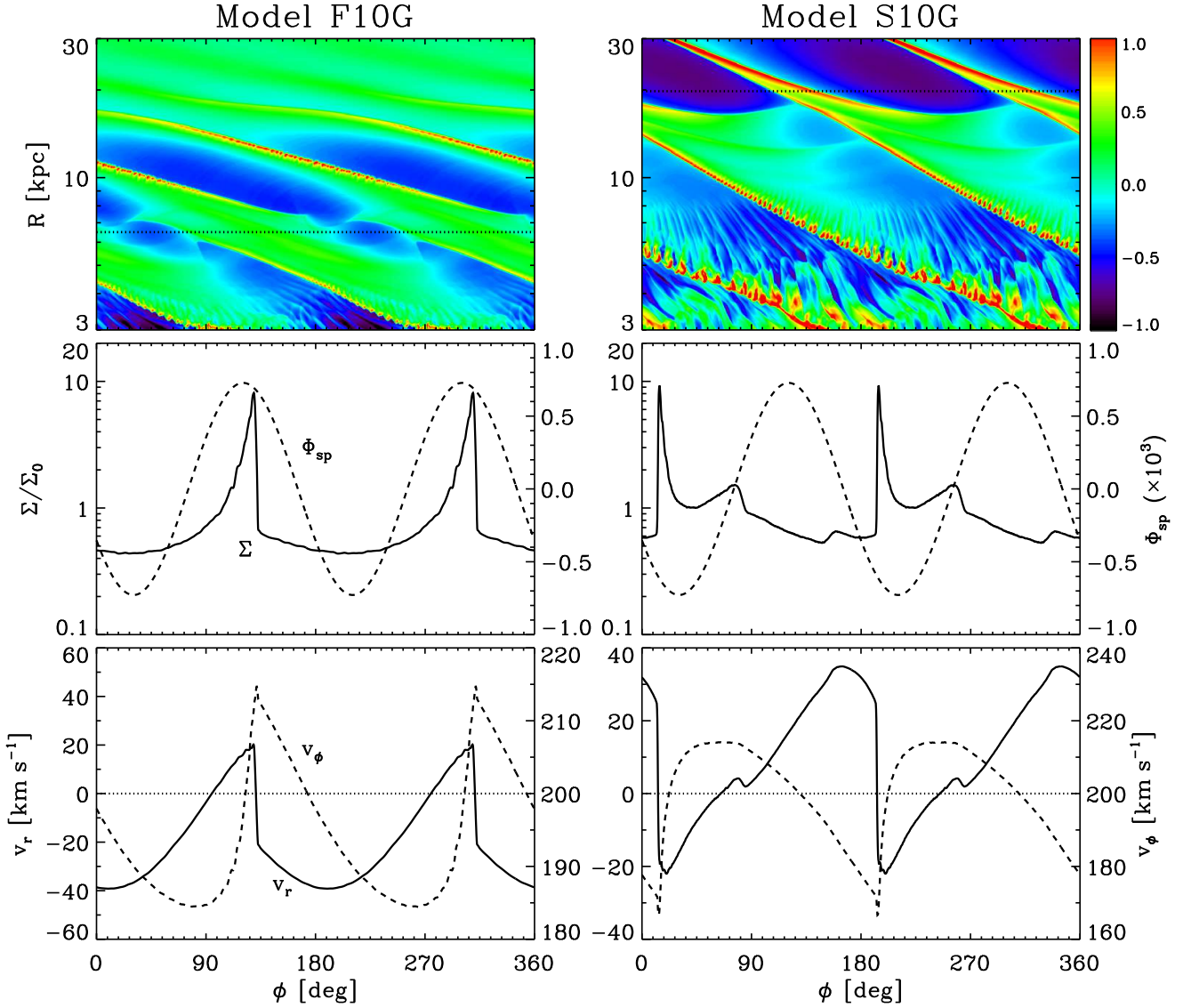


Figure 6. Top: Logarithm of the gas surface density on the $\log R$ - ϕ plane for Models (left) F10G and (right) S10G at $t = 0.4$ Gyr. The CR of the arms is indicated by a horizontal dotted line. Colorbar labels $\log(\Sigma/\Sigma_0)$. Middle: Azimuthal-cut profiles of the surface density Σ (solid; left y -axis) and the spiral potential Φ_{sp} (dashed; right y -axis) at $R = 13$ kpc. Bottom: The corresponding azimuthal profiles of the inertial-frame radial (solid; left y -axis) and azimuthal (dashed; right y -axis) velocities along the same cut.

by squares, is generated by the gas outside the CR rotating slower the pattern. In Model S10G, they become weaker with decreasing R from the outer boundary, move inward across the CR, and cease to exist at $R \sim 17$ kpc. In Model F10G and I10G, on the other hand, they are strongest at $R \sim 10$ kpc and 15 kpc, respectively, and do not extend inward across the CRs. In what follows, we term the first and second spiral shock the inner and outer shocks, respectively.

The extension of the spiral shocks across the CR in the S models is caused by epicycle motions of perturbed gas elements near the CR by the spiral potential. To illustrate this, we plot in Figure 5 instantaneous streamlines of the gas in Model S10G at $t = 0.4$ Gyr in the frame corotating with the spiral potential. Only a few streamlines around a Lagrangian point denoted by L_1 are shown. The spiral potential induces radial velocity perturbations with amplitude Δv_R in the

gas flows. In the local approximation, the corresponding radial amplitude of the epicycle orbits is $\Delta R = \Delta v_R / \kappa$ (e.g., Binney & Tremaine 2008). While a gas element originally located well inside the CR goes out radially on the course of its epicycle motion, it meets a shock at an oblique angle smaller than 90° due to fast rotation relative to the pattern, and moves radially inward after the shock, as exemplified by the streamline A. But, gas elements located closer to L_1 achieve larger epicycle phases, due to slower relative rotation, when they hit the shocks. Thus, the angles between the incident streamlines and the shock fronts can become larger than 90° , causing the streamlines B-E to bend radially outward after the shocks. These outwardly-moving gas elements increasingly find themselves in the regions with smaller κ , which in turn makes them move much farther than the original ΔR implies. Consequently, the inner spiral

shocks are smoothly extended to the outer radial boundary in the S models. Note that the dense arm gas outside the CR is bounded by two spiral shocks in these models.

Similarly, the outer spiral shocks extend inward across the CR in the S models, but in this case the radial excursion of the perturbed elements is quite limited because they feel larger κ as they move inward. In Model S10G, for instance, the radial velocity perturbations at $R = 20$ kpc is $\Delta v_R = 36 \text{ km s}^{-1}$. With $\kappa = 13 \text{ km s}^{-1} \text{ kpc}^{-1}$ at this radius, the radial displacement is $\Delta R = 2.7$ kpc, which matches the numerical results well. In the F and I models, however, $\Delta R \sim 0.1$ kpc due to larger κ , which is too small a perturbation to make spiral shocks extended across the CR.

Figure 6 plots the gas surface density in the $\log R$ - ϕ plane, together with the azimuthal cut profiles of various quantities at $R = 13$ kpc for Models F10G and S10G at $t = 0.4$ Gyr. Relative to the spiral potential, the gas at this radius in Model F10G (Model S10G) is moving in the negative (positive) ϕ -direction, forming shock fronts that are displaced by $\sim 80^\circ$ downstream ($\sim 20^\circ$ upstream) from the potential minima. The gas is compressed at the shock fronts, enhancing the surface density there, while reducing the velocity perpendicular to the shocks. The gas expands after the shock in order to follow quasi-periodic galaxy rotation. The constraint of the potential vorticity conservation requires the velocity parallel to the shock to increase after the shock front, resulting in shear reversal inside the gaseous arms with $\Sigma/\Sigma_0 > 2$ (e.g., Balbus 1988; Kim & Ostriker 2002). Streaming velocities due to the spiral shocks amount typically to ~ 40 – 60 km s^{-1} . The overall flow pattern is similar to the observed profiles associated with spiral arms in M51 (see, e.g., Fig. 6 of Shetty et al. 2007).

3.2.2 Pitch Angle

Figure 7 compares the azimuthal positions of the inner (pluses) and outer (squares) spiral shocks with the minima (solid lines) of the external potential for our fiducial models at $t = 0.4$ Gyr. Only the regions with $\alpha \geq 0.5$ are shown. The discontinuation of both inner and outer spiral shocks at the CR is evident in Model F10G, while the inner spiral shocks extend all the way to the outer boundary in Model S10G. The spiral shocks are approximately logarithmic in shape over a wide range of radii, with a pitch angle depending on Ω_p . In Model S10G, the spiral shocks are located very close to the potential minima and thus have a pitch angle of $p_{\text{gas}} \sim 17^\circ$, not much different from p_* . In Models F10G and I10G, on the other hand, the shock positions deviate considerably from the potential minima, resulting in much smaller pitch angles of $p_{\text{gas}} \sim 8^\circ$ and 10° , respectively.

The dependence of the shock positions relative to the potential minima is due to the tendency that stronger shocks form farther downstream (Kim & Ostriker 2002). As Figure 4c shows, spiral shocks in Model S10G have $\mathcal{M}_\perp \sim 5$ at $R \sim 7$ kpc and are located near the potential minima. As R increases, \mathcal{M}_\perp decreases and the shocks become weaker, moving slightly toward the upstream direction. In Model F10G, on the other hand, \mathcal{M}_\perp ($\propto R$ for large R) varies a lot with R , leading to fairly large variations in the shock positions. For instance, spiral shocks at $R = 8$ kpc have $\mathcal{M}_\perp = 2$ and are placed near the potential minima. At $R = 12$ kpc, $\mathcal{M}_\perp \sim 7$ and the shocks are displaced by 90° toward the

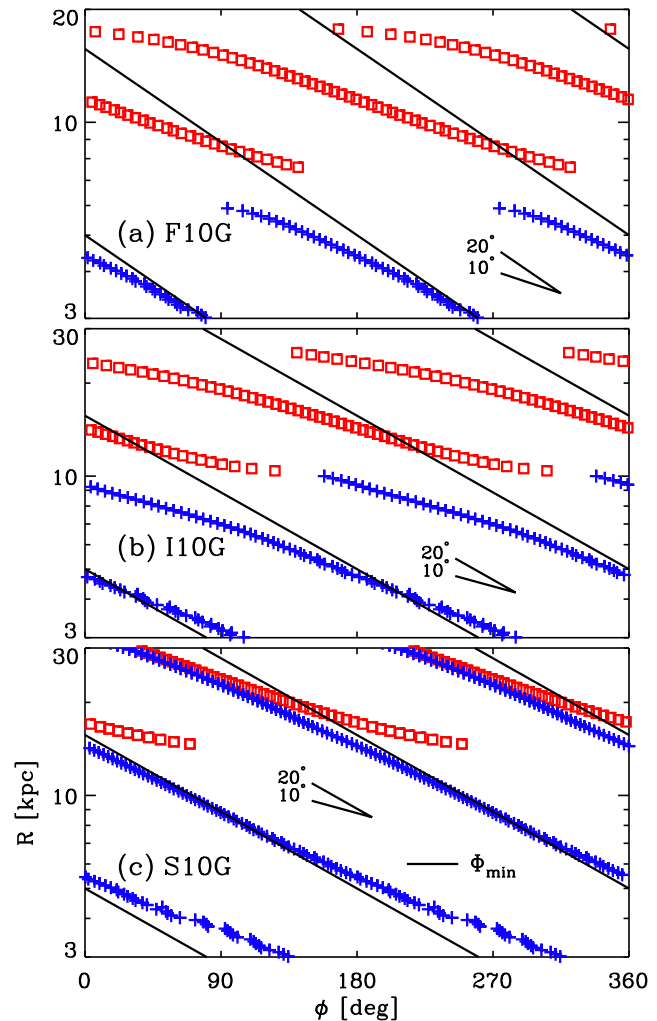


Figure 7. Azimuthal positions of the inner (pluses) and outer (squares) spiral shocks in comparison with the minimum loci (solid lines) of the spiral-arm potential for Models (a) F10G, (b) I10G, and (c) S10G at $t = 0.4$ Gyr. Only the regions with $\alpha \geq 0.5$ are shown. In (a) and (b), the azimuthal locations of spiral shocks change rapidly with R , resulting in a much smaller pitch angle than the stellar arms, while the difference between the pitch angles of the stellar and gaseous arms is small in (c).

downstream direction. At $R = 17$ kpc and beyond, $\mathcal{M}_\perp \gtrsim 12$ and no stationary configuration of spiral shocks can be found in this model.

The radial dependence of \mathcal{M}_\perp makes p_{gas} smaller than p_* . To quantify the offsets of the pitch angles, we define $\Delta p \equiv p_* - p_{\text{gas}}$, and plot them in Figure 8 as a function of the peak shock density Σ_{peak} for various models with differing \mathcal{F} and Ω_p . Each symbol gives the mean values of Δp and Σ_{peak} averaged over $t = 0.2$ – 0.6 Gyr and $R = 6$ – 15 kpc, with errorbars indicating the standard deviations. The dotted lines give our best fits

$$\Delta p = \begin{cases} 15 - 7 \log(\Sigma_{\text{peak}}/\Sigma_0), & \text{for F models,} \\ 12 - 5 \log(\Sigma_{\text{peak}}/\Sigma_0), & \text{for I models,} \\ 6 - 4 \log(\Sigma_{\text{peak}}/\Sigma_0), & \text{for S models.} \end{cases} \quad (9)$$

Since $\Delta p > 0$ for a reasonable range of Σ_{peak} , the pitch angle of the gaseous arms puts the lower limit to that of the

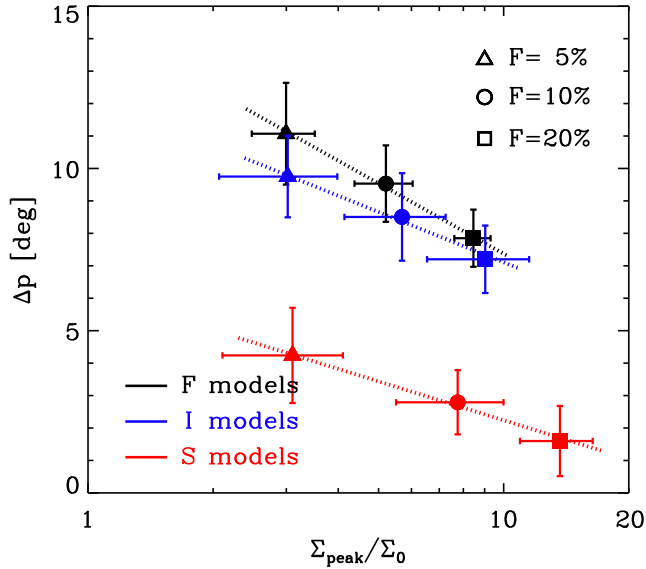


Figure 8. Offsets, $\Delta p = p_* - p_{\text{gas}}$, of the pitch angles between the stellar and gaseous arms as a function of the peak shock density Σ_{peak} averaged over $t = 0.2\text{--}0.6$ Gyr and $R = 6\text{--}15$ kpc for all self-gravitating models. Errorbars indicate the standard deviations in Δp and Σ_{peak} . The dotted lines are our best fits (Eq. [9]).

stellar arms. In general, larger Σ_{peak} corresponds to smaller Δp . Compared to the S models, models with larger Ω_p have larger Δp and smaller Σ_{peak} . Models with larger \mathcal{F} have smaller Δp and larger Σ_{peak} since a deeper spiral potential tends to form shocks closer to the potential minima. That the difference of Δp between the F and I models is smaller than that between the I and S models indicates that Δp is deeply related to R_{CR} . This result suggests that one should be cautious when inferring p_* from p_{gas} , especially when Ω_p is large and \mathcal{F} is small.

4 MASS DRIFT

The non-axisymmetric spiral pattern and the associated shocks are an efficient means of angular momentum transport, causing gas elements in orbital motions to move radially inward or outward depending on the sign of $\Omega - \Omega_p$ (e.g., Shu 1992). It is commonly accepted that inside the CR where $\Omega > \Omega_p$, gas can lose angular momentum from the spiral shocks, tending to move radially inward. Outside the CR with $\Omega < \Omega_p$, on the other hand, spiral shocks provide positive torque and thus cause the gas to move radially outward. In this section, we quantify the rate of mass drift driven by spiral arms.

To investigate the radial mass changes in our models, Figure 9 plots temporal variations of the total gas mass, $M(< 10\text{ kpc})$, within $R = 10$ kpc in various self-gravitating models. The presence of the spiral potential makes $M(< 10\text{ kpc})$ increase faster for models with stronger arms in the S models, while the F models with large \mathcal{F} exhibit decreases in $M(< 10\text{ kpc})$, corresponding to mass outflows. The I models do not show any noticeable secular changes in $M(< 10\text{ kpc})$ since the mass is measured near the CR. Figure 10 plots the radial distributions of the mass drift

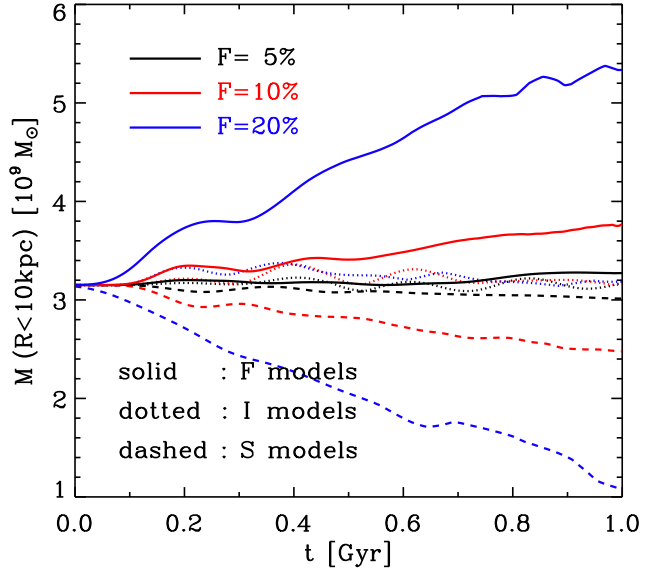


Figure 9. Temporal variations of the integrated mass $M(R < 10\text{ kpc})$ within 10 kpc for all self-gravitating models. Solid lines are for the S models exhibiting gas inflows, while dashed lines are for the F models with gas outflows. For the I models, $M(R < 10\text{ kpc})$ plotted as dotted lines does not change much over time.

rate, $\dot{M}_{\text{tot}}(R) \equiv -dM(< R)/dt$, averaged over $t = 0.2\text{--}0.8$ Gyr, for both self-gravitating (solid lines) and non-self-gravitating (dashed lines) models. The vertical bar marked by χ^2 in each panel indicates the typical standard deviations. Note that \dot{M}_{tot} is negative for mass inflows and positive for outflows. All the models show mass inflows inside the CR, with the effect of self-gravity insignificant except for Model S20G. In the S models, \dot{M}_{tot} is relatively constant at $\sim -(0.2\text{--}3) M_{\odot} \text{ yr}^{-1}$ over a wide range of R , which is significantly larger than $\sim -(0.05\text{--}0.8) M_{\odot} \text{ yr}^{-1}$ and $\sim -(0.1\text{--}1.2) M_{\odot} \text{ yr}^{-1}$ in the F and I counterparts, respectively, owing to larger R_{CR} . In contrast, the regions outside the CR clearly show mass outflows, with \dot{M}_{tot} varying with R considerably. Columns (2) and (3) of Table 2 list $\langle \dot{M}_{\text{tot}} \rangle_{\text{in}}$ and $\langle \dot{M}_{\text{tot}} \rangle_{\text{out}}$ averaged spatially over $R_{\text{ILR}} \lesssim R \lesssim R_{\text{CR}}$ and $R_{\text{CR}} \lesssim R \lesssim R_{\text{term}}$, respectively. Here, R_{term} represents the termination radius of the spiral shocks for the F and I models, as mentioned in Section 3.2.1, and is taken to 35 kpc for the S models.

The radial gas drift in our models is caused by the combination of three processes: (1) dissipation of angular momentum at spiral shocks, (2) torque by the external spiral potential, and (3) torque by the self-gravitational potential. The first two processes have previously been well recognized by other authors (e.g., Kalnajs 1972; Roberts & Shu 1972; Lubow et al. 1986; Hopkins & Quataert 2011), while the effect of self-gravity did not receive much attention. We thus write

$$\dot{M}_{\text{tot}} = \dot{M}_{\text{shock}} + \dot{M}_{\text{ext}} + \dot{M}_{\text{self}}, \quad (10)$$

where \dot{M}_{shock} , \dot{M}_{ext} , and \dot{M}_{self} denote the contributions of spiral shocks, the external spiral potential, and the gaseous self-gravity, respectively. It is well known that \dot{M}_{ext} can be expressed by

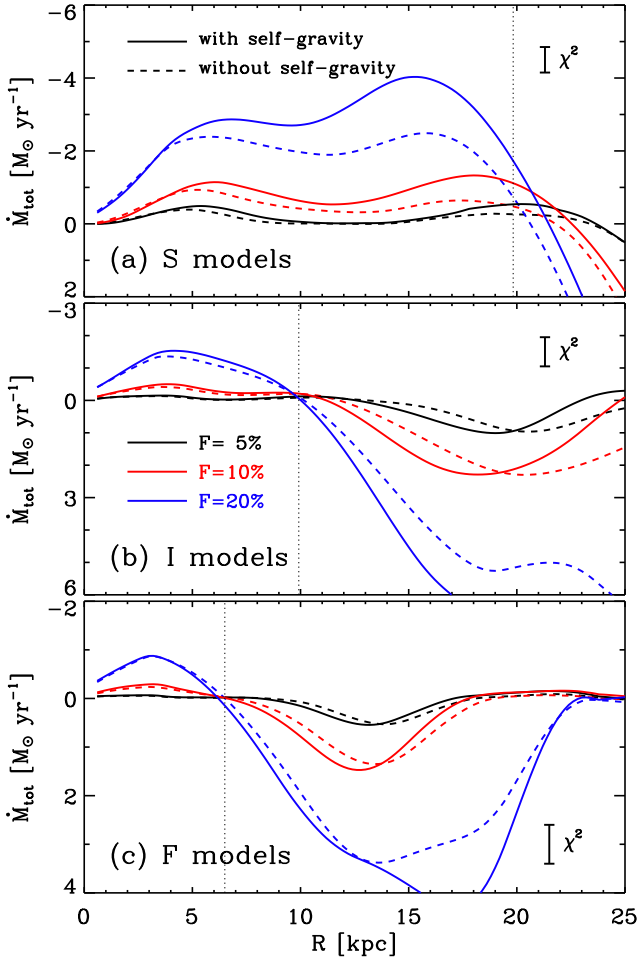


Figure 10. Radial dependence of the mass drift rate $\dot{M}_{\text{tot}} \equiv -dM(< R)/dt$ averaged over $t = 0.2\text{--}0.8$ Gyr for the (a) S (b) I, and (c) F models. The solid and dashed lines represent self-gravitating and non-self-gravitating models, respectively. The short vertical bars marked by χ^2 give the typical variations of \dot{M} over time. The vertical dotted line in each panel indicates the CR.

$$\dot{M}_{\text{ext}} = \left(\frac{1}{R} \frac{\partial R^2 \Omega}{\partial R} \right)^{-1} \int_{-\pi}^{\pi} \Sigma \frac{\partial \Phi_{\text{sp}}}{\partial \phi} d\phi, \quad (11)$$

(e.g., Lubow et al. 1986). We similarly write the self-gravitational contribution as

$$\dot{M}_{\text{self}} = \left(\frac{1}{R} \frac{\partial R^2 \Omega}{\partial R} \right)^{-1} \int_{-\pi}^{\pi} \Sigma \frac{\partial \Phi_{\text{gas}}}{\partial \phi} d\phi. \quad (12)$$

There is no simple analytic expression for \dot{M}_{shock} .

Using equations (11) and (12), we calculate \dot{M}_{ext} and \dot{M}_{self} from our numerical results, and then \dot{M}_{shock} from equation (10). Figure 11 plots the radial distributions of \dot{M}_{shock} , \dot{M}_{ext} , and \dot{M}_{self} from the self-gravitating, slow arm models. These values averaged over $R_{\text{ILR}} \lesssim R \lesssim R_{\text{CR}}$ or $R_{\text{CR}} \lesssim R \lesssim R_{\text{term}}$ are listed in Columns (4)–(9) of Table 2 for all the models. As expected, \dot{M}_{shock} is negative in most of the region inside the CR and positive outside the CR, although $\dot{M}_{\text{shock}} = 0$ does not correspond exactly to the CR. This is because the inner and outer spiral shocks extend across the CR, as explained in Section 3.2.1. Since the effect of the inner shocks is stronger on the mass drift than that of

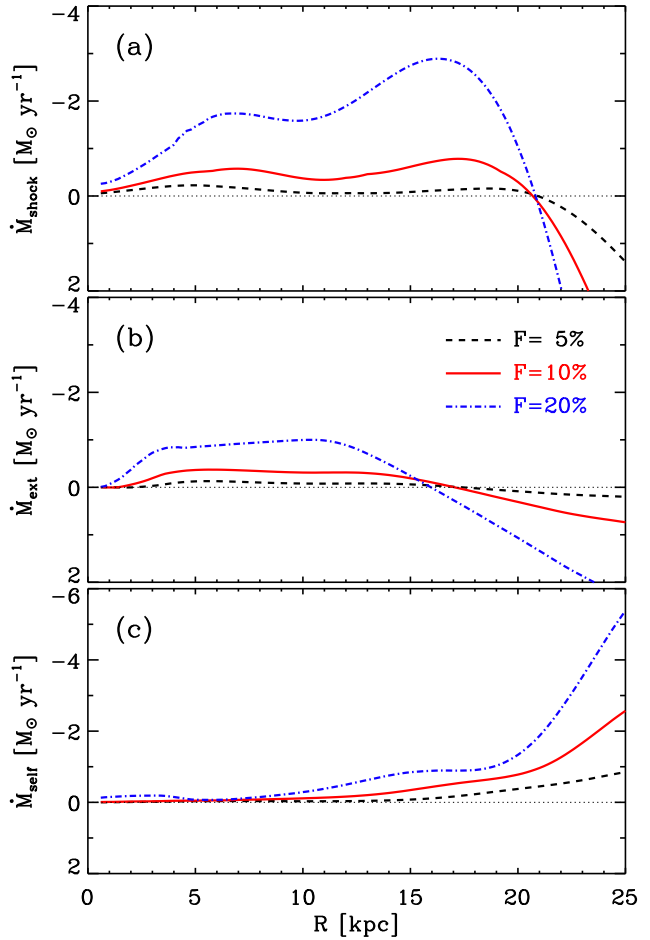


Figure 11. Radial distributions of (a) \dot{M}_{shock} , (b) \dot{M}_{ext} , and (c) \dot{M}_{self} for all self-gravitating, slow arm models, averaged over $t = 0.2\text{--}0.8$ Gyr. Models with stronger arms definitely have a higher mass drift rate. Note that \dot{M}_{shock} is negative inside the CR and positive outside the CR. The self-gravitational contribution which is always negative dominates at large R .

the outer shocks, $\dot{M}_{\text{shock}} = 0$ occurs at $R \sim 21$ kpc, roughly independent of \mathcal{F} , slightly outside the CR. Well inside the CR, \dot{M}_{ext} is negative mostly due to the torque on the gas in the postshock expanding zones rather than on the gas at the shock fronts. Although the latter has the highest density, its contribution to \dot{M}_{ext} turns out to be insignificant, except near the CR, since it is located very close to the potential minima in the S models. Near the CR, \dot{M}_{ext} becomes positive due to the torque on the gas at the shock fronts that are displaced substantially from the potential minima toward the upstream direction.

The self-gravitational torque overwhelms the other torques outside the CR. This is because self-gravity becomes relatively more important at larger R , as equation (6) suggests. In addition, gaseous arms in outer regions are bounded by two spiral shocks and thus relatively thick. Figure 12 compares the azimuthal distributions of gas surface density together with the spiral and self-gravitational potentials at (left) $R = 15$ kpc and (right) 25 kpc in Model S10G at $t = 0.4$ Gyr. The shock-bounded arms outside the CR form at the expense of lower interarm density and thus have

Table 2. Various Mass Drift Rates Induced by Spiral Arms

Model (1)	$\langle \dot{M}_{\text{tot}} \rangle_{\text{in}}$ (2)	$\langle \dot{M}_{\text{tot}} \rangle_{\text{out}}$ (3)	$\langle \dot{M}_{\text{shock}} \rangle_{\text{in}}$ (4)	$\langle \dot{M}_{\text{shock}} \rangle_{\text{out}}$ (5)	$\langle \dot{M}_{\text{ext}} \rangle_{\text{in}}$ (6)	$\langle \dot{M}_{\text{ext}} \rangle_{\text{out}}$ (7)	$\langle \dot{M}_{\text{self}} \rangle_{\text{in}}$ (8)	$\langle \dot{M}_{\text{self}} \rangle_{\text{out}}$ (9)
F05G	-0.054	0.273	-0.033	0.181	-0.018	0.101	-0.003	-0.010
F10G	-0.249	0.919	-0.126	0.518	-0.112	0.435	-0.011	-0.035
F20G	-0.781	2.479	-0.391	1.134	-0.274	1.552	-0.116	-0.207
I05G	-0.095	0.556	-0.057	0.414	-0.032	0.163	-0.006	-0.021
I10G	-0.361	1.730	-0.188	1.153	-0.153	0.663	-0.021	-0.087
I20G	-1.184	4.313	-0.600	2.415	-0.489	2.256	-0.095	-0.358
S05G	-0.205	1.032	-0.075	1.024	-0.079	1.167	-0.052	-1.159
S10G	-0.876	2.669	-0.391	2.185	-0.302	3.326	-0.181	-2.842
S20G	-3.074	6.244	-1.838	3.429	-0.799	7.537	-0.438	-4.722
<hr/>								
F05N	-0.046	0.226	-0.033	0.110	-0.012	0.116	0.0	0.0
F10N	-0.203	0.772	-0.120	0.321	-0.083	0.452	0.0	0.0
F20N	-0.778	2.280	-0.518	0.802	-0.260	1.478	0.0	0.0
I05N	-0.080	0.411	-0.054	0.221	-0.026	0.191	0.0	0.0
I10N	-0.292	1.322	-0.178	0.602	-0.114	0.720	0.0	0.0
I20N	-1.116	3.315	-0.694	1.199	-0.423	2.115	0.0	0.0
S05N	-0.159	0.665	-0.111	0.024	-0.048	0.641	0.0	0.0
S10N	-0.608	2.889	-0.404	0.764	-0.204	2.125	0.0	0.0
S20N	-2.240	6.952	-1.552	1.489	-0.688	5.463	0.0	0.0

Note. – All values are averaged over $0.2 \text{ Gyr} \leq t \leq 1.0 \text{ Gyr}$ and in units of $M_{\odot} \text{ yr}^{-1}$. Columns (2), (4), (6), and (8) are the mass drift rates averaged over $R_{\text{ILR}} \lesssim R \lesssim R_{\text{CR}}$, while Columns (3), (5), (7), and (9) are the values averaged over from the CR to the termination radius of the spiral shocks.

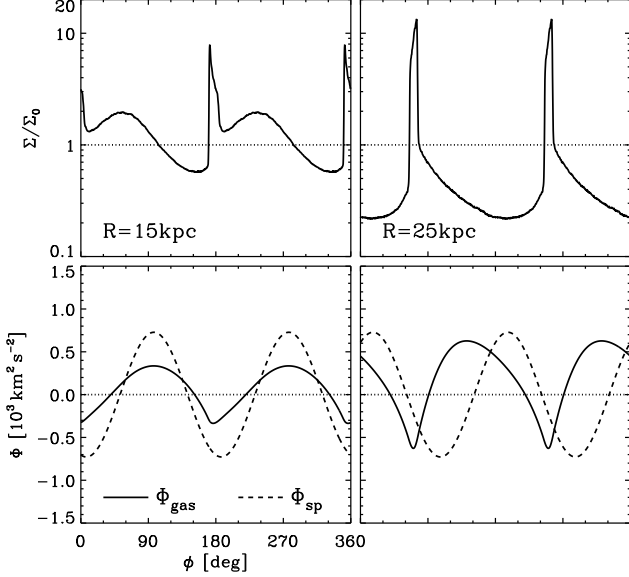


Figure 12. Azimuthal distributions of (upper panels) gas surface density and (lower panels) the spiral and self-gravitational potentials at $R = 15$ and 25 kpc for Model S10G when $t = 0.4 \text{ Gyr}$. Note that gaseous arms outside the CR have larger density contrasts and thus produce stronger self-gravitational forces than inside the CR.

stronger self-gravitational forces, compared to those inside the CR. Note that the density distribution at $R = 25 \text{ kpc}$ is slightly asymmetric with respect to the minima of Φ_{gas} , with larger density at the side with $\partial\Phi_{\text{gas}}/\partial\phi < 0$. The corresponding self-gravitational torque is thus negative over most of the simulation domain.

A stronger spiral potential leads to larger $|\dot{M}_{\text{tot}}|$. Our numerical results for the mass drift for all self-gravitating models can be fitted as

$$\langle \dot{M}_{\text{tot}} \rangle_{\text{in}} \approx \begin{cases} -4\mathcal{F}(0.2 + 4\mathcal{F})(\Sigma/\Sigma_0), & \text{for F models,} \\ -5\mathcal{F}(0.2 + 5\mathcal{F})(\Sigma/\Sigma_0), & \text{for I models,} \\ -7\mathcal{F}(0.2 + 10\mathcal{F})(\Sigma/\Sigma_0), & \text{for S models,} \end{cases} \quad (13)$$

and

$$\langle \dot{M}_{\text{tot}} \rangle_{\text{out}} \approx \begin{cases} 5\mathcal{F}(1 + 7\mathcal{F})(\Sigma/\Sigma_0), & \text{for F models,} \\ 5\mathcal{F}(2 + 11\mathcal{F})(\Sigma/\Sigma_0), & \text{for I models,} \\ 5\mathcal{F}(4 + 11\mathcal{F})(\Sigma/\Sigma_0), & \text{for S models,} \end{cases} \quad (14)$$

in units of $M_{\odot} \text{ yr}^{-1}$, both of which are accurate within $\sim 0.1 M_{\odot} \text{ yr}^{-1}$ for $0.05 \leq \mathcal{F} \leq 0.2$. In these models, the angular momentum loss at spiral shocks, the external gravitational torque, and the self-gravitational torque account for about 50%, 40%, and 10% of the total, on average, respectively, roughly independent of \mathcal{F} . In the S models, the corresponding radial inflow velocity is $v_d = \dot{M}_{\text{tot}}/(2\pi R\Sigma_0) \sim 1 \text{ km s}^{-1}$ at $R = 10 \text{ kpc}$, with the associated timescale comparable to the Hubble time.

5 LINE-OF-SIGHT VELOCITY

The distribution of line-of-sight velocities in the plane of sky can be a useful diagnostic tool in analyzing the gas kinematics in disk galaxies. Figure 13 plots the synthetic, projected maps of (upper panels) the gas surface density in logarithmic scales, and (lower panels) the line-of-sight velocity V_{LOS} for (left) Models F10G and (right) S10G at $t = 0.4 \text{ Gyr}$. Only the regions with $\Sigma/\Sigma_0 \geq 1$ are shown to mimic strong radio emissions from overdense regions. The galaxy is rotating in the counterclockwise direction. In each panel, the disk is assumed to be inclined arbitrarily by 65° with respect to the

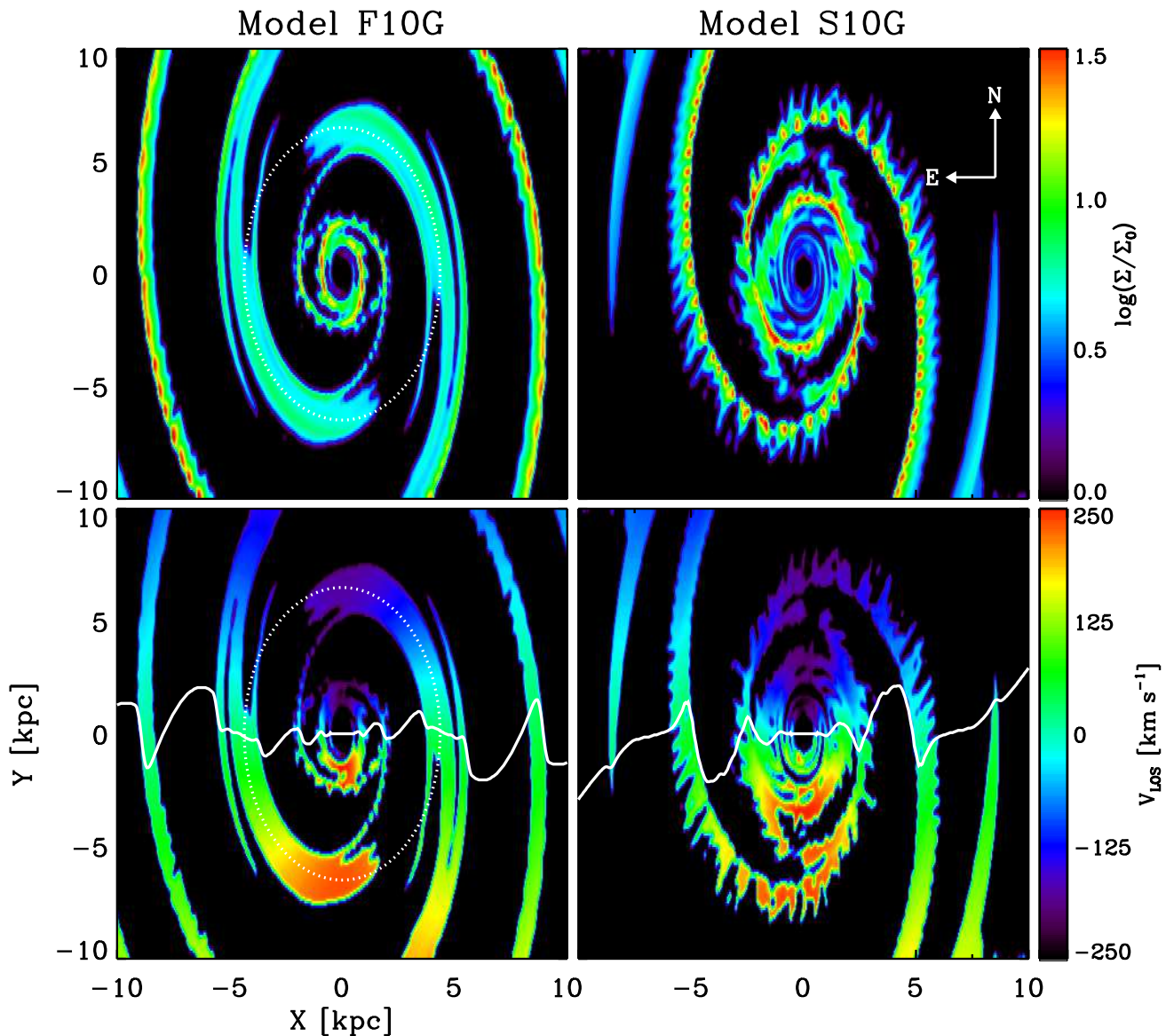


Figure 13. Synthetic, projected maps of (upper panels) gas surface density Σ in logarithmic scale and (lower panels) the line-of-sight velocity V_{LOS} for Models (left) F10G and (right) S10G at $t = 0.4$ Gyr. Only the regions with $\Sigma/\Sigma_0 \geq 1$ are shown. The inclination angle of the disk is set to 65° relative to the plane of the sky, and the position angle of the arms at $R = 5$ kpc is taken to be -25° from the north. The dotted ellipses in the left panels indicate the location of the CR in Model F10G. The solid curves in the lower panels draw the loci of $V_{\text{LOS}} = 0$. Upper and lower colorbars label $\log(\Sigma/\Sigma_0)$ and V_{LOS} in units of km s^{-1} , respectively.

plane of sky (XY -plane) such that west of the disk is the near side. We choose -25° as the position angle of the arms at $R = 5$ kpc measured from the north (positive Y -axis). The dotted ovals in the left panels indicate the location of the CR in Model F10G, while the solid curves in the lower panels draw the loci of $V_{\text{LOS}} = 0$. Density and velocity data are smoothed by a Gaussian beam with a width of 0.12 kpc. The colorbars label $\log(\Sigma/\Sigma_0)$ and V_{LOS} in units of km s^{-1} .

In the central regions at $R \lesssim 2$ kpc, the zero velocity curve runs almost parallel to the nodal line (X -axis) for both models. As R increases, however, the pattern speed makes several differences in the arm morphologies and the distribution of V_{LOS} that can possibly be discerned observationally. First, gaseous arms are more tightly wound in Model F10G

due to a rapid change in \mathcal{M}_\perp than in Model S10G. Second, spiral arms located outside the CR are bounded by shock fronts at the outer edges, while those inside the CR are shocked at the inner edges. Consequently, the gas density in the arms is distributed asymmetrically along a radial cut such that it is larger at smaller R outside the CR and at larger R inside the CR, as the upper panels of Figure 13 illustrate. Third, gas streaming motions associated with spiral shocks amount to ~ 40 – 60 km s^{-1} , which can make the gas rotate slower than the pattern even inside the CR (see Fig. 6). Thus the zero velocity curve near the western (eastern) arm in Model S10G strongly bends downward (upward), toward the opposite direction to the galaxy rotation. On the other hand, the gas rotates faster than the pattern

outside the CR, which causes the zero velocity curve to bend upward near the arms in the western parts of the disk, as in Model F10G. These differences can be used to determine whether observed segments of the arms are located inside or outside the CR. We will discuss this further in application to NGC 3627 in Section 6.2.

6 SUMMARY AND DISCUSSION

6.1 Summary

We have presented the results of grid-based hydrodynamic simulations on spiral structures and radial mass drift in disk galaxies driven by spiral arms. The gaseous disk is assumed to be infinitesimally thin, unmagnetized, isothermal with the sound speed of $c_s = 10 \text{ km s}^{-1}$, and initially uniform with surface density $\Sigma_0 = 10 M_\odot \text{ pc}^{-2}$. For the spiral arms, we impose a rigidly-rotating logarithmic gravitational potential with pitch angle $p_* = 20^\circ$, strength \mathcal{F} , and pattern speed Ω_p . To study the dependence of the shock structure and the mass drift rates on \mathcal{F} and Ω_p , we consider three types of models in which the arm is rotating fast at $\Omega_p = 30 \text{ km s}^{-1} \text{ kpc}^{-1}$, intermediately at $\Omega_p = 20 \text{ km s}^{-1} \text{ kpc}^{-1}$, or slow at $\Omega_p = 10 \text{ km s}^{-1} \text{ kpc}^{-1}$, which are referred to as the F, I, and S model, respectively. We also vary \mathcal{F} between 5 and 20%. The main results of this paper are summarized as follows.

1. *Extent of Spiral shocks.* – The radial extent of spiral shocks depends rather sensitively on the arm pattern speed. In the F and I models, spiral shocks exist only up to $R_{\text{term}} \sim 17 \text{ kpc}$ and $\sim 25 \text{ kpc}$, respectively, while the outer region is almost featureless other than weak trailing waves. This is because when equation (8) is not fulfilled, gas perturbed by one arm does not have sufficient time to adjust itself to the imposed spiral potential before encountering the next arm. That is, the rapid rotation of the potential makes itself effectively smoothed considerably along the azimuthal direction, and gas moves almost ballistically (Baker & Barker 1974). In the S models, on the other hand, the whole disk satisfies $\mathcal{M}_\perp / \sin p_* \lesssim 20$ and forms spiral shocks across the entire simulation domain. In these models with a slow pattern, spiral shocks are not terminated at the CR due to epicycle motions of perturbed gas elements. Since a gas element on its epicycle orbit achieves larger (smaller) amplitudes as it moves radially outward (inward), the spiral shocks produced inside the CR are able to extend all the way to the outer radial boundary, while those originally formed outside the CR extend only slightly inward of the CR. As a consequence, the dense arm gas outside the CR is bounded by two spiral shocks in the S models.

2. *Relation between the pitch angle and shock strength.* – In a quasi-steady state, stronger spiral shocks tend to form at farther downstream relative to the minima of the imposed spiral potential. Since \mathcal{M}_\perp varies systematically with R , this makes the pitch angle p_{gas} of the gaseous arms smaller than that of the stellar arms. In our models, the offset between p_{gas} and p_* amounts to $\sim 2^\circ$ – 12° , and is larger for smaller \mathcal{F} since a deeper potential tends to have shocks closer to its minima. It is also larger for models with larger Ω_p due to larger radial variations of \mathcal{M}_\perp . Equation (9) gives our fits to $\Delta p = p_* - p_{\text{gas}}$ against the peak shock density Σ_{peak} of the gaseous spiral arms.

3. *Mass Drift* – The non-axisymmetric spiral potential is an efficient means of angular momentum transport, initiating radial drift of gas that would otherwise be in circular motions. In our models, the radial mass drift is caused by a combination of three processes: angular momentum loss at spiral shocks, external gravitational torque, and self-gravitational torque. While self-gravitational torque is always negative, it is usually smaller than the other torques inside the CR. On the other hand, the direction of the mass drift by the shock loss and external torque depends on the sign of $\Omega - \Omega_p$, such that it is radially inward inside the CR and outward outside the CR. The resulting mass inflow rate, averaged over $R_{\text{ILR}} \lesssim R \lesssim R_{\text{CR}}$, is in the range $\langle \dot{M}_{\text{tot}} \rangle_{\text{in}} \sim -(0.05\text{--}3.0) M_\odot \text{ yr}^{-1}$, with a larger value corresponding to stronger and/or slower arms, as described by equation (13). The shock loss and external spiral potential account for about 50% and 40% of the total, respectively.

4. *Line-of-Sight Velocity* – Since the spiral arms cause streaming motions in the gas flows whose amplitudes depend on the arm pattern speed, the related line-of-sight velocity V_{LOS} and the density distribution across the arms can potentially provide information on the arm pattern speed. Gaseous arms located outside the CR have a larger density at larger R along a radial cut. In this case, the gas in the arms rotates faster than the pattern due to the streaming motions, tending to make the locus of $V_{\text{LOS}} = 0$ bend in the same way as the direction of galaxy rotation. In contrast, gaseous arms located inside the CR have a larger density at smaller R , and the $V_{\text{LOS}} = 0$ curve near the arms bends in the opposite sense to the galaxy rotation (see Fig. 13).

6.2 Discussion

Our result that the radial extent of gaseous arms depends on the arm pattern speed is overall consistent with the finding of Patsis et al. (1994) who showed using SPH simulations that gaseous spirals exist up to the CR when Ω_p is large ($\sim 37.4 \text{ km s}^{-1} \text{ kpc}^{-1}$), while they extend to the end of the stellar spiral arms when Ω_p is small ($\sim 12.5 \text{ km s}^{-1} \text{ kpc}^{-1}$). Patsis et al. (1994) further found that an oval ring forms, possibly by the resonance, near the OLR area. A similar ring-like structure forms in the outer regions of Model I10G at late time when the outer ends of trailing gaseous arms curve back radially inward to touch the other arms (see Fig. 2). The main difference in the model parameters between our and their models is the pitch angle of the stellar potential. To explore the effect of p_* on the position of ring-like structures that form, we have run two additional models with $p_* = 30^\circ$ and 44° , while the other parameters remain identical to Model I10G.³ Figure 14 plots the distributions of surface density at $t = 1 \text{ Gyr}$ from these additional runs as well as Model I10G. In each panel, the dotted and solid circles mark the CR and OLR, respectively. An oval-like structure forms in all models, although its size tends to decrease with increasing p_* . Model I10G with $p_* = 20^\circ$ has an oval-like structure well outside the OLR, while it is coincidentally at the OLR. Since the arm termination (and thus the ring formation) occurs at the radius where equation (8) is satisfied,

³ Models in Patsis et al. (1994) took $p_* = 44^\circ$.

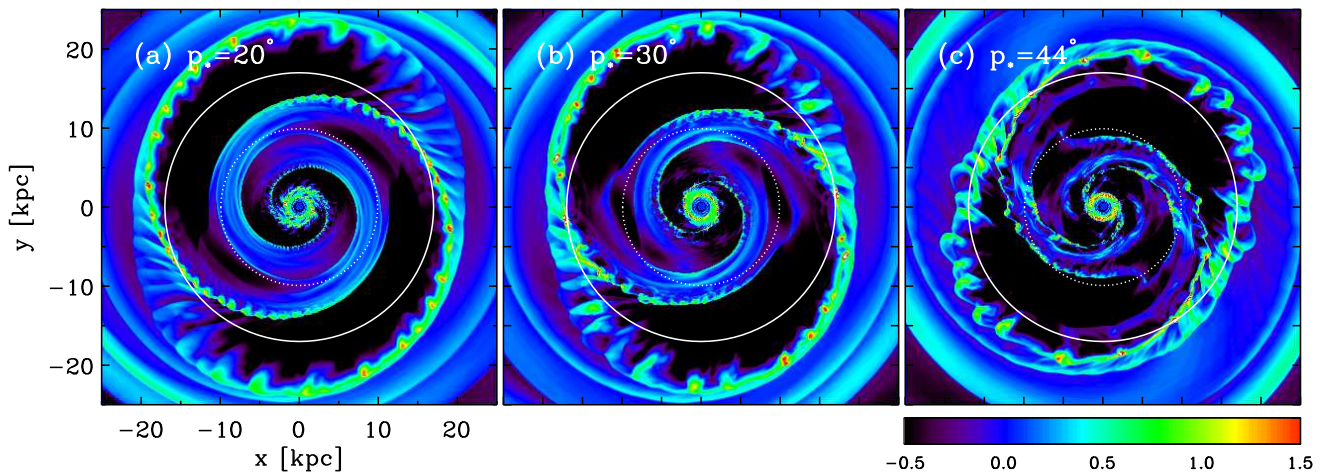


Figure 14. Logarithm of gas surface density at $t = 1.0$ Gyr for self-gravitating models with pitch angle (a) $p_* = 20^\circ$, (b) $p_* = 30^\circ$, and (c) $p_* = 44^\circ$. The other parameters are the same as in Model I10G. In each panel, the dotted and solid circles draw the CR and OLR. A ring-like structure forms near the position where the outer end of a gaseous arm curls radially in to be connected to the other arm. Colorbar labels $\log(\Sigma/\Sigma_0)$.

one can expect a smaller ring when p_* is larger, fully consistent with our numerical results. This demonstrates that the formation of a ring-like structure near or beyond the OLR is not due to the resonance.

It is interesting to apply our results to the spatial extent of observed arms in the barred-spiral galaxy M83. In this galaxy, the spiral pattern rotates relatively rapidly at $\Omega_p \approx 45 \text{ km s}^{-1} \text{ kpc}^{-1}$ and has a pitch angle of $p_* \approx 16^\circ$ (e.g., Lord & Kenney 1991; Zimmer et al. 2004). The rotational velocity at the flat part is $\sim 180 \text{ km s}^{-1}$ (Lundgren et al. 2004), so that the CR is located at $\sim 4 \text{ kpc}$, corresponding to $\sim 3'$ at the distance of 4.5 Mpc (Thim et al. 2003). The radio data of Lundgren et al. (2004) show that the gaseous arms are weaker at the CR than at the neighboring arms, similarly to our results shown in Figure 4. The arms extend up to $\sim 6'$, while there is a plenty of gas with $\Sigma \sim 2 M_\odot \text{ pc}^{-2}$ in the outer regions where the gaseous arms are absent (Crosthwaite et al. 2002; Lundgren et al. 2004). Although the termination radius of the gaseous arms in M83 is close to the OLR, it is uncertain whether the OLR plays a central role in limiting the arm extent. We note that the radius of $6'$ corresponds to $\mathcal{M}_\perp / \sin p_* \sim 23\text{--}30$ for the observed CO velocity dispersions of $c_s \sim 7.8 \pm 0.9 \text{ km s}^{-1}$ (Lundgren et al. 2004), suggesting that the idea of arm termination by too large \mathcal{M}_\perp is not inconsistent with the observed gaseous arms in M83 with $\mathcal{F} \sim 5\text{--}10\%$.

To measure the mass drift rate unaffected by a radial density gradient for given \mathcal{F} , we have employed simple disk models with radially constant Σ_0 and \mathcal{F} . In models with a slow pattern speed, this inevitably results in readily discernible spiral shocks all the way to the outer radial boundary. In reality, however, gas surface density in spiral galaxies appears to drop off exponentially or more rapidly (e.g., Bigiel & Blitz 2012). In addition, the stellar spiral potential is likely to become shallower with increasing R beyond the CR (e.g., Contopoulos & Grosbøl 1986, 1988; Patsis et al. 1991). Although arm-to-interarm density contrasts are likely unchanged by the background density (especially when self-gravity is unimportant), small values of Σ_0 and \mathcal{F} would

make it difficult to detect gaseous spiral arms at large radii in real spiral galaxies.

The tendency of spiral shocks moving toward the upstream direction with increasing R was reported by Gittins & Clarke (2004), and our results further show that the displacement of spiral shocks is larger when Ω_p is larger. This is consistent with the results of Patsis et al. (1994) who found that gaseous arms are much tighter than the stellar pattern in their high- Ω_p models. Gittins & Clarke (2004) also noted that in addition to stellar and gaseous arms, there are star-forming arms traced by HII regions, all of which may have different pitch angles such that $p_* > p_{\text{gas}} > p_{\text{SF}}$ if the time offset between the gaseous and star-forming arms is independent of R . Indeed, Grosbøl & Patsis (1998) showed that the stellar arms traced by K' -band observations are more loosely wound than the optical arms for a sample of five galaxies. Although Davis et al. (2012) more recently found that the arm pitch angles in the optical band are almost identical to those in the near-IR band within observational uncertainties (see also Seigar et al. 2006), their fitting results plotted in their Figure 13 still show that the latter is larger by $\sim 2^\circ$ than the former for $p_* \sim 10^\circ\text{--}30^\circ$, consistent with our numerical results. Martínez-García (2012) also reported that arm pitch angles are larger in the H -band than in the B -band. More accurate observational estimates are required to explore the dependence on Ω_p of the offsets between arm pitch angles in different wavelength bands.

In application to the gas accretion in the Milky Way, Lubow et al. (1986) used a local model of spiral shocks by considering the reaction of stellar waves back to the gaseous self-gravity and calculated the mass inflows rate due to the spiral shocks and external gravitational torque. They found that the total inflow rate is in the range $\dot{M} \sim -(0.2\text{--}0.4) M_\odot \text{ yr}^{-1}$ for $\mathcal{F} = 3\%$, consistent with the extrapolation of our numerical results. They also found that the external potential is about three times more effective than the viscous torque, which is different from our finding that the effect of the spiral shocks in removing angular momentum is slightly larger than that of the external potential. This dif-

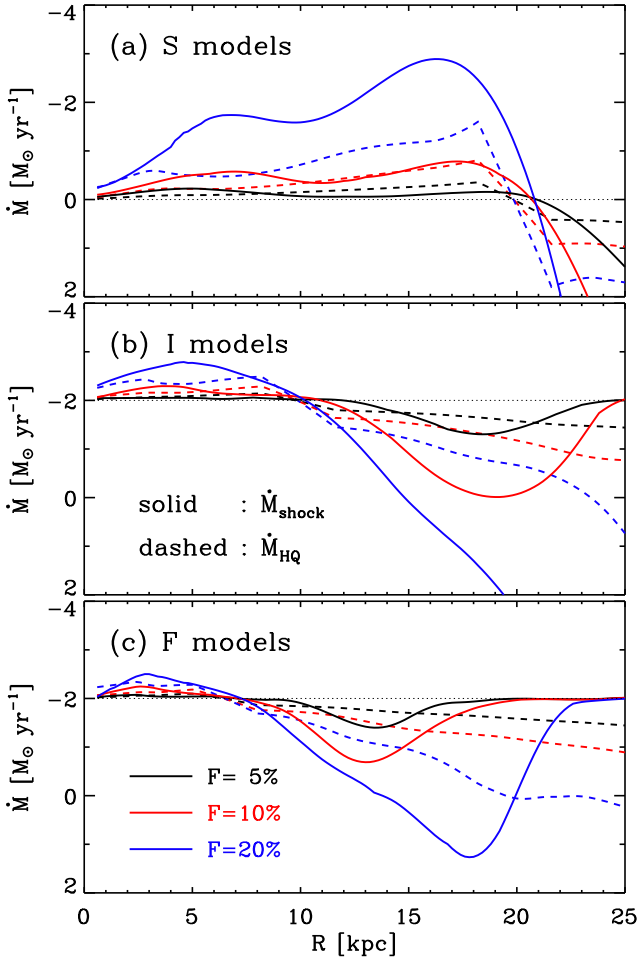


Figure 15. Comparison of the mass inflow rate \dot{M}_{shock} (solid lines) by angular-momentum loss at spiral shocks in our models with the analytic estimate \dot{M}_{HQ} of Hopkins & Quataert (2011) (dashed lines) given by equation (15) for the (a) S, (b) I, and (c) F models. Note that \dot{M}_{HQ} agrees approximately with \dot{M}_{shock} only in the S models with small \mathcal{F} , while it differs considerably from \dot{M}_{shock} for the small- Ω_p with large \mathcal{F} and all the large- Ω_p models.

ference is presumably caused by the fact that Lubow et al. (1986) included physical viscosity accounting for cloud collisions. This smears out the shocks and moves the peak density toward downstream (see also Kim et al. 2008, 2010), which tends to enhance the external torque and reduce the angular-momentum loss at the shock fronts.

Hopkins & Quataert (2011) put forward a simple analytic model for angular momentum transport and related gas inflows driven by a non-axisymmetric stellar potential. By neglecting the effects of thermal pressure as well as the flow velocity relative to the potential, they considered orbit crossing of collisionless particles as a criterion for shock formation and derived the mass inflow rate

$$\dot{M}_{\text{HQ}} = -\bar{\Sigma} R^2 \Omega \mathcal{F} \tan p_* \text{sign}(\Omega - \Omega_p) |f(\zeta)|, \quad (15)$$

where $\bar{\Sigma}$ is the azimuthally-averaged gas density and $f(\zeta)$ denotes the correction factor of order unity for the degree of the orbit crossing, ζ . They confirmed that equation (15) is in good agreement with their numerical results when bar-like

stellar modes dominate the perturbations. To check whether equation (15) is also good for the cases dominated by a spiral potential, Figure 15 compares \dot{M}_{HQ} (dashed lines) with \dot{M}_{shock} (solid lines) from our numerical simulations. Note that equation (15) can be a good approximation for the mass inflows due to the shock loss *alone*, only for weak spiral shocks in the S models in which shock fronts are located very close to the potential minima. On the other hand, equation (15) fails to describe the mass drift accurately for the slow-arm models with large \mathcal{F} and for the F models where spiral shocks are displaced significantly from the potential minima. In this case, the shock formation requires consideration of thermal pressure as well as incident velocities, which were neglected in Hopkins & Quataert (2011).

By analyzing Sloan Digital Sky Survey DR7 data, Comerón et al. (2009) found that about 20% of 266 galaxies with measured bar strength host dust lanes. On the other hand, numerical simulations with only a bar potential without spiral arms show that dust lanes remain strong only for 0.1 Gyr around the time when the bar potential achieves its full strength (e.g., Kim et al. 2012b; Kim & Stone 2012). This implies that barred galaxies with strong dust lanes should be either dynamically young or supplied with fresh gas. Our numerical results in this paper suggest that spiral arms can be efficient to transport gas from outside to the central region provided that the spiral arms have quite a low pattern speed so as to have a large CR radius.

In addition to enhancing the mass in the central region, mass inflows by spiral arms also may help to increase the rate of star formation occurring in the nuclear ring induced by a bar potential. Seo & Kim (2013) numerically found that without spiral arms or gas infall from halo, the star formation rate in nuclear rings decays to small values below $\sim 1 M_{\odot} \text{ yr}^{-1}$ after showing a strong burst that lasts only about 0.1 Gyr. This is in contrast to the claim that star formation in nuclear rings is a long-lived phenomenon ($\sim 1\text{--}2$ Gyr), with multiple episodes (e.g., Allard et al. 2006; Sarzi et al. 2007; van der Laan et al. 2013). In Model S10G, gas flows radially inward at a rate $\dot{M}_{\text{tot}} \sim -1.0 M_{\odot} \text{ yr}^{-1}$ at $R = 5$ kpc, which would fuel star formation on the galactic center when enough mass is accumulated to undergo gravitational collapse. It would be interesting to study how much star formation is enhanced in nuclear rings by an addition of outer spiral arms, which will direct our future research.

By employing a simple isothermal equation of state, our models produce spiral shocks with quite a large density contrast between arm and interarm regions. For instance, Shetty et al. (2007) reported that spiral arms seen in CO observations of M51 typically have an arm-to-interarm density contrast of ~ 5 , while it is ~ 20 in our models (see, e.g., Fig. 6). Even considering the beam smearing of the CO data, the density contrast in our models seems to be larger than observed values. In real galaxies, there are many physical processes including magnetic fields and star formation that can affect spiral-shock gas dynamics considerably. Magnetic fields that are pervasive in the interstellar medium (e.g., Beck 1996; Fletcher et al. 2011) can make the isothermal gas behave as if it were adiabatic with index of 2 for one-dimensional compression (e.g., Shu 1992), reducing the arm-peak density substantially (e.g., Kim & Ostriker 2002; Kim et al. 2002; Lee & Shu 2012). Star formation and ensuing feedback occurring inside spiral arms is able to provide

the arm gas with turbulent kinetic energy which not only tends to disperse dense gas but also triggers new star formation (e.g., Mac Low & Klessen 2004; McKee & Ostriker 2007; Shetty & Ostriker 2012; Kim et al. 2013). A reduced arm density may decrease the mass drift rate, while magnetic fields themselves can be a source of additional angular momentum transport via tension forces. Therefore, more realistic quantitative assessment of the mass drift rate caused by spiral arms requires consideration of these processes as well as radiative heating and cooling.

Finally, we discuss the distribution of gas density and V_{LOS} in the arms found in our models in comparison with observations. Regan et al. (2002) presented a velocity map of CO emission from the barred-spiral galaxy NGC 3672, derived from Gaussian fits to the line profiles. Their Figure 6 shows that the observed distributions of V_{LOS} in the outer regions, especially the loci of $V_{\text{LOS}} = 0$, match those in Model S10G better than in Model F10G presented in Figure 13, suggesting that the spiral arms in NGC 3672 are located inside the their CR. A close inspection of Figure 4a of Regan et al. (2002) (see also Figure 1c of Chemin et al. 2003) reveals that the density profiles of the gaseous arms along a radial cut have a steeper gradient at the inner edge than the outer edge, which also hints that the spiral arms rotate slow. Since the CR of a strong bar is placed just outside the bar end, these all indicate that the spiral arms in NGC 3672 have a lower pattern speed than the bar. Indeed, Rand & Wallin (2004) used the method of Tremaine & Weinberg (1984) to show that the bar in NGC 3627 has a pattern speed of $\Omega_b = 50^{+3}_-8 \text{ km s}^{-1} \text{ kpc}^{-1}$, while the southern extension of the western spiral arm has $\Omega_p = 23 \pm 4 \text{ km s}^{-1} \text{ kpc}^{-1}$. The corresponding CR radii of the bar and arms are at $R = 1.3'$ and $3.3'$, respectively, indicating that the observed spiral arms in Regan et al. (2002) are located in between the CRs of the bar and spiral arms, consistent with kinematic features in our models.

ACKNOWLEDGMENTS

We gratefully acknowledge helpful discussions with Bruce G. Elmegreen and Eve C. Ostriker. We are also grateful to the referee for an insightful and constructive report. This work was supported by the National Research Foundation of Korea (NRF) grant funded by the Korean government (MEST), No. 2010-0000712. The computation of this work was supported by the Supercomputing Center/Korea Institute of Science and Technology Information with supercomputing resources including technical support (KSC-2012-C3-19). Hospitality at APCTP during the 7th Korean Astrophysics Workshop is kindly acknowledged.

REFERENCES

- Allard E. L., Knapen J. H., Peletier R. F., & Sarzi M. 2006, *MNRAS*, 371, 1087
- Amaral L. H., & Lépine J. R. D. 1997, *MNRAS*, 286, 885
- Ann H. B., & Thakur P. 2005, *ApJ*, 620, 197
- Artymowicz P., & Lubow S. H. 1992, *ApJ*, 389, 129
- Athanassoula E. 1992, *MNRAS*, 259, 345
- Athanassoula E. 2002, *ApJ*, 569, L83
- Baker P. L., & Barker P. K. 1974, *A&A*, 36, 179
- Balbus S. A. 1988, *ApJ*, 324, 60
- Beck R. 1996, *ARAA*, 34, 155
- Bertin G., & Lin C. C. 1996, *Spiral Structure in Galaxies: A Density Wave Theory* (Cambridge: MIT Press)
- Bertin G., Lin C. C., Lowe S. A., & Thustans R. P. 1989a, *ApJ*, 338, 78
- Bertin G., Lin C. C., Lowe S. A., & Thustans R. P. 1989b, *ApJ*, 338, 104
- Bigiel F., & Blitz L. 2012, *ApJ*, 756, 183
- Binney J., & Tremaine S. 2008, *Galactic Dynamics* (2nd ed.; Princeton, NJ: Princeton Univ. Press)
- Bournaud F., & Combes F. 2002, *A&A*, 392, 83
- Brunett M., Chiappini C., & Pfenniger D. 2011, *A&A*, 534, 44
- Buta R. 2013, *Secular Evolution of Galaxies: XXIII Canary Islands Winter School of Astrophysics*, eds. J. Falcon-Barroso, & J. Knapen (Cambridge: Cambridge University Press), in press; arXiv:1304.3529
- Buta R., & Combes F. 1996, *Fund. Cosmic Phys.*, 17, 95
- Chakrabarti S., Laughlin G., & Shu F. H. 2003, *ApJ*, 596, 220
- Chemin L., Cayatte V., Balkowski C., Marcelin M., Amram P., van Driel W., & Flores H. 2003, *A&A*, 405, 89
- Colella P., & Woodward P. R. 1984, *Comput. Phys.*, 54, 174
- Comerón S., Martínez-Valpuesta I., Knapen J. H., & Beckman J. E. 2009, *ApJ*, 706, L256
- Comerón S., Knapen J. H., Beckman J. E., Laurikainen E., Salo H., Martínez-Valpuesta & Buta R. J. 2010, *MNRAS*, 402, 2462
- Contopoulos G., & Grosbøl P. 1986, *A&A*, 155, 11
- Contopoulos G., & Grosbøl P. 1986, *A&A*, 197, 83
- Crosthwaite L. P., Turner J. L., Buchholz L., Ho P. T. P., & Martin R. N. 2002, *AJ*, 123, 1892
- Davis B. L., Berrier J. C., Shields D. W., et al. 2012, *ApJS*, 199, 33
- Dobbs C. L., & Bonnell I. A. 2006, *MNRAS*, 367, 873
- Dobbs C. L., Burkert A., & Pringle J. E. 2011, *MNRAS*, 417, 1318
- Donner K. J., & Thomasson M. 1994, *A&A*, 290, 785
- Dwarkadas V. V., & Balbus S. A. 1996, *ApJ*, 467, 87
- Elmegreen B. G. 1995, *Molecular Clouds and Star Formation*, ed. C. Yuan & H. You (Singapore: World Scientific), p. 149
- Englmaier P., & Gerhard O. 1997, *MNRAS*, 287, 57
- Fathi K., Beckman J. E., Piñol-Ferre N., Hernandez O., Martínez-Valpuesta I., & Carignan C. 2009, *ApJ*, 704, 1657
- Fletcher A., Beck R., Shukurov A., Berkhuijsen E. M., & Horellou C. 2011, *MNRAS*, 412, 2396
- Foyle K., Rix H.-W., & Zibetti S. 2010, *MNRAS*, 407, 2010
- García-Burillo S., Fernández-García S., Combes F., et al. 2009, *A&A*, 496, 85
- Gittins D. M., & Clarke C. J. 2005, *MNRAS*, 349, 909
- Gómez G. C., & Cox D. P. 2002, *ApJ*, 580, 235
- Gómez G. C., Pichardo B., & Martos M. A. 2013, *MNRAS*, 430, 3010
- Grosbøl P. J., & Patsis P. A. 1998, *A&A*, 336, 840
- Haan S., Schinnerer E., Emsellem E., García-Burillo S., Combes F., Mundell C. G., & Rix H.-W. 2009, *ApJ*, 692, 1623

- Hanawa T., & Kikuchi D. 2012, ASP Conference Series V. 459: Numerical Modeling of Space Plasma Flows: ASTRONOM-2011, eds. N. V. Pogorelov, J. A. Font, E. Audit, & G. P. Zank (ASP: San Francisco), p. 310
- Heller C. H., & Shlosman I. 1994, ApJ, 424, 84
- Hopkins P., & Quataert E. 2011, MNRAS, 415, 1027
- Hunt L. K., et al. 2009, ApJ, 482, 133
- Jogee S., Scoville N., & Kenney J. D. P. 2005, ApJ, 630, 837
- Kalnajs A. J. 1971, ApJ, 166, 275
- Kalnajs A. J. 1972, ApJ, 11, L41
- Knapen J. H., Shlosman I., & Peletier R. F. 2000, ApJ, 529, 93
- Kim C.-G., Kim W.-T., & Ostriker E. C. 2008, ApJ, 681, 1148
- Kim C.-G., Kim W.-T., & Ostriker E. C. 2010, ApJ, 720, 1454
- Kim C.-G., Ostriker E. C., & Kim W.-T. 2013, ApJ, 776, 1
- Kim W.-T., & Ostriker E. C. 2002, ApJ, 570, 132
- Kim W.-T., & Ostriker E. C. 2006, ApJ, 646, 213
- Kim W.-T., & Ostriker E. C. 2007, ApJ, 660, 1232
- Kim W.-T., Ostriker E. C., & Stone J. M. 2002, ApJ, 581, 1080
- Kim W.-T., & Stone J. M. 2012, ApJ, 751, 124
- Kim W.-T., Seo W.-Y., Stone J. M., Yoon D., & Teuben P. J. 2012, ApJ, 747, 60
- Kim W.-T., Seo W.-Y., & Kim Yonghwi 2012b, ApJ, 758, 14
- Kormendy J., & Kennicutt R. C. 2004, ARA&A, 42, 603
- Lacey C. G., & Fall S. M. 1985, ApJ, 290, 154
- Laurikainen E., Salo H., Buta R., & Vasylyev S. 2004, MNRAS, 355, 1251
- Lee W.-K., & Shu F. H. 2012, ApJ, 756, 45
- Lin C. C., & Lau Y. Y. 1979, St. A. M., 60, 97
- Lin C. C., & Shu F. H. 1964, ApJ, 140, 646
- Lin C. C., & Shu F. H. 1966, Proc. Natl. Acad. Sci., 55, 229
- Lord S. D., & Kenney J. D. P. 1991, ApJ, 381, 130
- Lubow S. H., Balbus S. A., & Cowie L. L. 1986, ApJ, 309, 496
- Lundgren A. A., Olofsson H., Wiklund T., & Rydbeck G. 2004, A&A, 422, 865
- Lynden-Bell D., & Kalnajs A. J. 1972, MNRAS, 157, 1
- Maciejewski W. 2004, MNRAS, 354, 892
- Mac Low M., & Klessen R. S. 2004, RvMP, 76, 125
- Martínez-García E. E. 2012, ApJ, 744, 92
- Martínez-García E. E., & González-Lópezlira R. A. 2011, ApJ, 734, 122
- Martos M., Hernandez X., Yáñez M., Moreno E., & Pichardo B. 2004, MNRAS, 350, L47
- McKee C. F., & Ostriker E. C. 2007, ARA&A, 45, 565
- Oh S. H., Kim W.-T., Lee H. M., & Kim J. 2008, ApJ, 683, 94
- Patsis P. A., Contopoulos G., & Grosbøl P. 1991, A&A, 243, 373
- Patsis P. A., Hiotelis N., Contopoulos G., & Grosbøl P. 1994, A&A, 286, 46
- Patsis P. A., Grosbøl P., & Hiotelis N. 1997, A&A, 323, 762
- Patsis P. A., & Athanassoula E. 2000, A&A, 358, 45
- Piner B. G., Stone J. M., & Teuben P. J. 1995, ApJ, 449, 508
- Rand R. J., & Wallin J. F. 2004, ApJ, 614, 142
- Rautiainen P., & Salo H. 1999, A&A, 348, 737
- Regan M. W., & Mulchaey J. S. 1999, AJ, 117, 2676
- Regan M. W., Sheth K., Teuben P. J., & Vogel S. N. 2002, ApJ, 574, 126
- Roberts W. W. 1969, ApJ, 158, 123
- Roberts W. W., & Shu F. H. 1972, ApJ, 12, 49
- Roca-Fàbrega S., Valenzuela O., Figueras F., Romero-Gómez M., Velázquez H., Antoja T., & Pichardo B. 2013, MNRAS, 432, 2878
- Roškar R., Debattista V. P., Quinn T. R., Stinson G. S., & Wadsley J. 2008, ApJ, 684, L79
- Sanders R. H., & Huntley J. M. 1976, ApJ, 209, 53
- Sarzi M., Allard E. L., Knapen J. H., & Mazzuca L. M. 2007, MNRAS, 380, 949
- Seigar M. S., Bullock J. S., Barth A. A., & Ho L. C. 2006, ApJ, 645, 1012
- Sellwood J. A. 2011, MNRAS, 410, 1637
- Sellwood J. A. 2013, to appear in Reviews of Modern Physics; arXiv:1310.0403
- Sellwood J. A., & Binney J. J. 2002, MNRAS, 336, 785
- Sellwood J. A., & Sparke L. S. 1988, MNRAS, 231, 25
- Seo W.-Y., & Kim W.-T. 2013, ApJ, 769, 100
- Shetty R., & Ostriker E. C. 2006, ApJ, 647, 997
- Shetty R., & Ostriker E. C. 2008, ApJ, 684, 978
- Shetty R., & Ostriker E. C. 2012, ApJ, 754, 2
- Shetty R., Vogel S. N., Ostriker E. C., & Teuben P. J. 2007, ApJ, 665, 1138
- Shlosman I., Begelman M. C., & Frank J. 1990, Nature, 345, 679
- Shu F. H. 1992, The Physics of Astrophysics. II. Gas Dynamics (Mill Valley: Univ. Science Books)
- Slyz A. D., Kranz T., & Rix H.-W. 2003, MNRAS, 346, 1162
- Thakur P., Ann H. B., & Jiang I. 2009, ApJ, 693, 586
- Thim F., Tammann G. A., Saha A., et al. 2003, ApJ, 590, 256
- Toomre A. 1964, ApJ, 139, 1217
- Toomre A. 1981, in Structure and Evolution of Normal Galaxies, ed. S. M. Fall & D. Lynden-Bell (Cambridge: Cambridge Univ. Press), p. 111
- Tremaine S., & Weinberg M. D. 1984, ApJ, 282, L5
- van der Laan T. P. R., Schinnerer E., Emsellem E., et al. 2013, A&A, 551, 81
- van de Ven G., & Fathi K. 2010, ApJ, 723, 767
- Wada K. 2008, ApJ, 675, 188
- Wada K., & Koda J. 2004, MNRAS, 349, 270
- Wada K., Baba J., & Saitoh T. R. 2011, ApJ, 735, 1
- Yáñez M. A., Norman M. L., Martos M. A., & Hayes J. C. 2008, ApJ, 672, 207
- Zhang X. 1996, ApJ, 457, 125
- Zimmer P., Rand R. J., & McGraw J. T. 2004, ApJ, 607, 285

This paper has been typeset from a \TeX / \LaTeX file prepared by the author.